RSC Advances

PAPER

View Article Online
View Journal | View Issue

Cite this: *RSC Adv.*, 2024, **14**, 9725

Synergistic effect of KI on the corrosion inhibition of a poly(diallylammonium chloride)-based cyclocopolymer containing bis-cationic motifs for mild steel corrosion in 20% formic acid†

Lipiar K. M. O. Goni,[a] Ibrahim Y. Yaagoob,[a] Mohammad A. J. Mazumder *[ab] and Shaikh A. Ali *[ab]

This study entails the syntheses of a homopolymer, poly(diallylammonium chloride) (**3**), and copolymers (**8a–c**) containing hydrophilic/hydrophobic pendants and their role in mitigating mild steel in aggressive 20% formic acid, a type of corrosion that is not frequently discussed in the literature. The synthesized homopolymer and copolymers were characterized by FTIR, NMR, viscometry, and TGA. Inhibitor **8b** was found to be the most potent, with 81.8% inhibition efficiency (IE) registered *via* the potentiodynamic polarization method for 100 ppm of inhibitor concentration at 30 °C. Inhibitor **8b**, mixed with 2 mmol KI, showed more than 90% IE for a meager 1 ppm inhibitor concentration. For a synergism of 50 ppm inhibitor and 2 mmol KI, the IE reached a high value of 99.1%. The synergism was so good that it helped the inhibitor retain ~100% of its original IE even after a 24 h weight loss study at 60 °C. The adsorption isotherm study showed that **8b** followed the Langmuir adsorption isotherm and adsorbed *via* chemisorption. A very high value (2.48×10^5 L mol^{-1}) of the equilibrium adsorption constant (K_{ads}) indicated strong adsorption. XPS and SEM surface studies provided evidence of the inhibitor found on the metal surface. Some toxicological parameters, such as LC50, bioaccumulation factor, and developmental toxicity, have been measured computationally. A brief mechanistic insight into how the inhibitors functioned has been offered along with the DFT study.

Received 30th December 2023
Accepted 16th March 2024

DOI: 10.1039/d3ra08959b

rsc.li/rsc-advances

1. Introduction

The phenomenon of corrosion happens when metals lose electrons upon reacting with a corrosive environment, causing the metals to degrade and ensuing materials and economic losses and claiming lives at times.[1,2] Scientifically, corrosion is regarded as an exchange of electrons happening at the interface between a metal and solution.[3] It has become an extraordinarily pervasive and perennial problem. Any nation worldwide reportedly spends 5–10% of its GNP on corrosion-related costs.[2] It was revealed that the world had to spend 3.4% of its total GDP on the cost of corrosion in 2013.[4] Several strategies, namely coating, cathodic or anodic protection, corrosion inhibition, *etc.*, are available to combat corrosion. However, corrosion inhibitors are hugely popular and in-demand approaches.[5–7] These substances significantly reduce corrosion when added to a corrosive metal solution. Mild steel has enormous implications in industrial set-ups, and is used to construct machinery parts, pipelines, railways, automobile body parts, *etc.*, owing to its favorable mechanical properties and affordable costs.[8] As such, mild steel corrosion study is of great importance.

Corrosion caused by organic acids isn't discussed as much as that caused by mineral acids. Even though organic acids have many implications across many industries, the corrosion they cause hasn't been studied widely.[9] Carboxylic acids in the form of acetic acid, formic acid, *etc.*, can incur corrosion damage on various metals, such as nickel, copper, zinc, *etc.*, in many indoor atmospheric environments. In many industries, the out-gassing of organic constituents, followed by their gradual oxidation to carboxylic acid, generates these acids.[10] Organic acids are weaker than mineral acids but can still be corrosive.[11] In oil and gas industries, acidizing is sometimes done where an acidic solution, such as hydrochloric, acetic, formic, sulfamic acid, *etc.*, is injected to promote good productivity. The acids are generally used in the 5–35% concentration range. However, even though this highly concentrated acid injection crushes the mineral build-up in the rocky matrix to boost the well capacity, the metallic components of the process become highly prone to severe corrosion damage from the aggressivity of the acid.[12]

[a]*Chemistry Department, King Fahd University of Petroleum & Minerals, Dhahran 31261, Saudi Arabia. E-mail: jafar@kfupm.edu.sa; Fax: +(966) 13 860 4277; Tel: +(966) 13 860 7836*

[b]*Interdisciplinary Research Center for Advanced Materials, King Fahd University of Petroleum & Minerals, Dhahran 31261, Saudi Arabia*

† Electronic supplementary information (ESI) available. See DOI: https://doi.org/10.1039/d3ra08959b

Therefore, adding inhibitors to the acidic solution is vital in this process. Furthermore, formic acid corrosion has been reported to have happened during the oxidation and burning of methanol fuel, which has been deemed cleaner and quite popular.[13] Therefore, formic acid corrosion across many industries can't be ignored.

Organic compounds that consist of heteroatoms, lone pairs, π-electrons, multiple bonds, and/or aromatic functionalities adsorb very well on the metal surface.[14] Polymers have multiple adsorption centers and an immense ability to cover the metal surface. In addition, nitrogenous compounds are found to be excellent inhibitors because they can trigger physical and chemical adsorption.[2] Studies have shown that polymeric surfactants are very effective in arresting corrosion.[15–19] The hydrophilic portions of the surfactants interact with the metal surfaces, and the hydrophobic parts spread out toward the water molecules and repel them. This study explores the mild steel corrosion inhibition efficiency of a homopolymer (**3**), poly(diallylammonium chloride), and some copolymers (**8a–c**) containing pyrrolidine ring and a long hydrophobic/hydrophilic cationic pendant (5–20%) moieties (Scheme 1) in a 20% formic acid solution. We found earlier that homopolymer (**3**), poly(diallylammonium chloride), was very efficient in inhibiting 1 M HCl-induced 304L stainless steel corrosion at 30 °C, a condition different from the current one in terms of the electrolyte and metal specimen.[20] The rationale behind orchestrating the homopolymer (**3**) with hydrophilic/hydrophobic pendant is founded upon the facts that nitrogen-containing imidazoles, long-chain aliphatic diamines, and quaternary ammonium-based compounds best tackle the acid-induced and underground pipeline corrosions.[21,22] Furthermore, when the same hydrophilic/hydrophobic pendant was added to poly(methyldiallylammonium chloride), a variant of homopolymer (**3**), the resulting co-polymeric corrosion inhibitor retarded CS 1018 corrosion in 15% HCl by >99%.[23] Therefore, this gave us the impression that modifying homopolymer (**3**) with that hydrophilic/hydrophobic pendant will produce a new, robust, and very efficient co-polymeric corrosion inhibitor to be studied for organic acid corrosion.

As per the recent awareness raised in terms of using conventional, toxic corrosion inhibitors harmful to both human beings and the environment, the current trends in the study of corrosion inhibitors are all about designing, developing, and synthesizing corrosion inhibitors with variable functional motifs (quaternary ammonium salts) that are environmentally benign. A corrosion inhibitor can be declared non-toxic based on several indices, such as environmental toxicity, bio-accumulation, biodegradability, *etc.* International commissions like Oslo and Paris (OSPAR) and Registration, Evaluation, Authorization, and Restriction of Chemicals (REACH) set these parameters.[24] The current study aims to cover extensive theoretical investigation to declare the studied corrosion inhibitors safe and non-toxic.

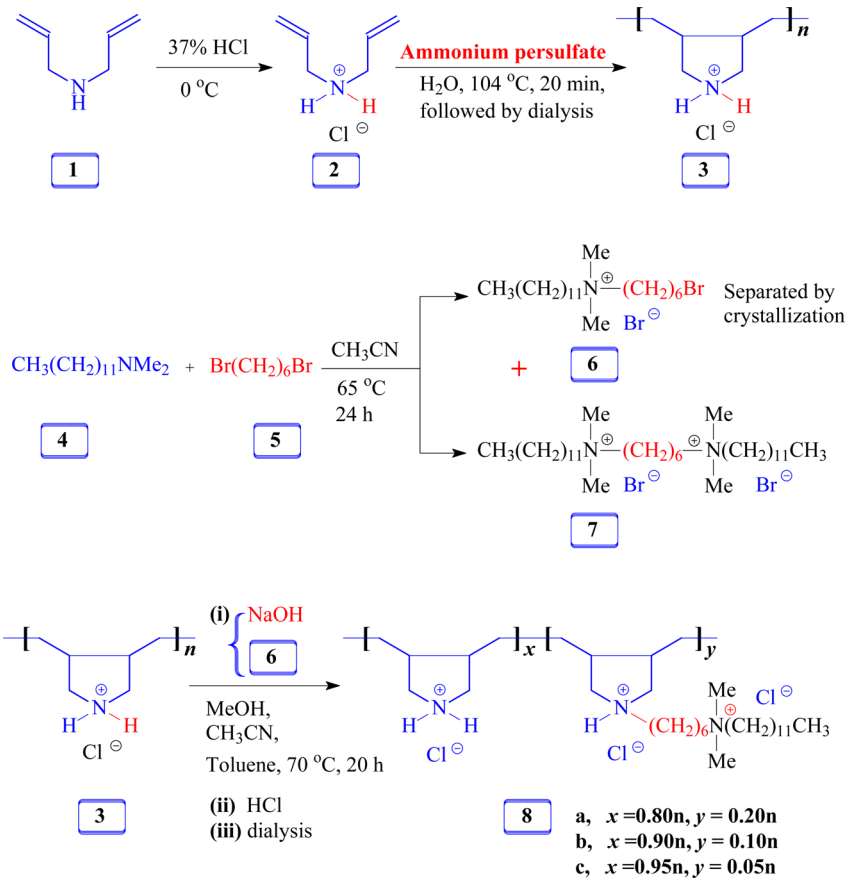

Scheme 1 Synthesis of the diallylamine salt-based monomer cyclopolymers.

Recently, the synergism of corrosion inhibitors with additives to combat corrosion has become a very useful trend, as it helps reduce the required dosage of corrosion inhibitors and widens their applications in a range of corrosive media. It has been reported that halide ions help organic inhibitors adsorb onto metal surfaces and improve their inhibitive effects.[25,26] Solomon and Umoren studied the synergism of polypropylene glycol (PPG) and KI for mild steel corrosion in 0.5 M H_2SO_4.[27] Adding 5 mM KI to 1000 ppm of PPG improved the IE from 83.8% to 98.7%. In another study, the same authors showed an impressive increase in IE for adding 2 mM KI to 1000 ppm of poly(methacrylic acid) (PMAA). While 1000 ppm of PMAA showed only 56.0% IE for mild steel corrosion in 0.5 M H_2SO_4, the IE increased to 95.9% for a mixture of 1000 ppm of PMAA and 2 mM KI.[28] Ansari *et al.* studied the anticorrosive effect of polyethyleneimine-grafted graphene oxide (PEI-GO) towards carbon steel corrosion in 15% HCl. While 100 ppm of PEI-GO imparted a maximum IE of 90.46%, a blend of 5 mM KI and 50 ppm of PEI-GO improved it to 95.77%.[29] Sovizi and Abbasi showed that the addition of 5 mM KI to 0.5 g L^{-1} of carboxymethyl cellulose (CMC) improved the IE from 65.2 to 80.4% for aluminium corrosion in 2 M H_2SO_4.[30] Haladu *et al.* studied the anticorrosion behavior of a cyclic cationic polymer (CCP) for low carbon steel corrosion in 15% HCl. Without adding KI, CCP imparted a maximum IE of 73.3% for a very high concentration of 500 ppm. However, when 5 mM KI was added, the IE improved to 95.1%.[31]

In this study, the inhibitory potential of inhibitor **8b** showed the highest inhibitory potential *via* gravimetric weight loss analysis. Several corrosion measurement techniques, both gravimetric and electrochemical, were employed to study the synergistic effects of the corrosion inhibitor. A computational analysis DFT was utilized to realize the mechanical and interactive functions of the corrosion inhibitors.

2. Experimental

2.1 Materials

Diallylamine (**1**), *N*,*N*-dimethyldodecylamine (**4**), ammonium persulfate (APS), and 1,6-dibromohexane (**5**) were purchased from Sigma-Aldrich. Spectra/Por membrane (MWCO: 3.5 kDa) from Spectrum Laboratories Inc. was used to dialyze the synthesized polymers. Mild steel metal samples were obtained from Chrome Contracting Ltd, Riyadh, Saudi Arabia. The composition (wt%) of the mild steel samples was as follows: C (0.21%), Si (0.29%), P (0.06%), Mn (0.49%), S (0.05%), Cu (0.06%), and Fe (balance). The test solution (20% formic acid) was prepared from 98% formic acid purchased from Sigma-Aldrich.

2.2 Physical methods

The measurement of the atomic compositions was carried out by an elemental analyzer (2400 Series II CHNS/O Analyzer – PerkinElmer). The recording of the IR spectra was conducted by an FTIR spectrometer (PerkinElmer 16F PC). A 400-MHz Bruker Avance III spectrometer was utilized to record ^{1}H- and ^{13}C-NMR spectra using CD_3OD and D_2O as the solvents. HOD and ^{13}C dioxane signals at δ 4.65 and 67.4 ppm were used as a reference, respectively. An Ubbelohde viscometer with a viscometer constant of 0.005 cSt s^{-1} was used to measure the viscosities at 30.0 ± 0.1 °C under N_2- and CO_2-free water conditions.

2.3 Polymer synthesis

2.3.1 Synthesis of diallylammonium chloride (2) and its cyclopolymerization to (3). 11.7 g (120 mmol) of ice-cold diallylamine (**1**) was taken in a round-bottom (RB) flask (200 mL). 13.8 g (140 mmol) of 37% conc. HCl was added dropwise under stirring. The resulting solution contained 16.0 g (120 mmol) of diallylammonium chloride **2** in water. Thereafter, the temperature of the RB flask, fitted with a condenser, was raised to 104 °C under N_2. Subsequently, the APS initiator (5 × 500 mg) was added in five steps, with the interval being 2 min between each step. The temperature of the reaction mixture was maintained for 20 min after an exothermic polymerization ensued. A dialysis tube of MWCO 3.5 kDa was used to dialyze the resultant thick liquid against distilled water for 12 h. The dialyzed solution was freeze-dried to afford polymer **3** as a white solid (14.0 g, 87%). ν_{max} (KBr): 3573, 2926, 2722, 2076, 1627, 1467, 1390, 1266, 1106, 1051, 971, 896, and 617 cm^{-1}. FTIR spectrum is displayed in Fig. S1 (ESI).†

Additionally, monomers as white crystals were obtained in a separate experiment by freeze-drying an aqueous solution of **2**. δ_H (D_2O) 3.44 (4H, d, *J* 6.4 Hz), 5.27 (4H, m), 5.69 (2H, m); δ_C (D_2O) 49.49 (2C), 124.62 (2C), 128.19 (2C), (dioxane: δ 67.4 ppm).

2.3.2 Synthesis of quaternary ammonium bromide (6). 12.8 g (60 mmol) of amine **4** and 73.2 g (300 mmol) of 1,6-dibromohexane **5** were added to acetonitrile (100 mL). The temperature of the reaction mixture was raised to 65 °C and stirred under N_2 for 24 h. After acetonitrile was removed, the excess of dibromohexane was removed under reduced pressure. The residual mixture was washed with ether (50 mL) in two steps and later dissolved in 50 mL of hot acetone. A white solid (2.5 g, 12%) was found after bis-quaternary salt **7** crystallized upon cooling of the ether-washed reaction mixture. When acetone was removed from the filtrate, mono-cationic salt **6** was found to be a white solid (22.5 g, 82%). MP 58–59 °C. (Found: C 52.2; H 9.6; N 3.0%. $C_{20}H_{43}Br_2N$ requires C 52.52; H 9.48; N 3.06%); ν_{max} (KBr): 3409, 2920, 2855, 1465, 1242, 1143, 1053, 964, 893, 779, 728, 637, 497, and 472 cm^{-1}. FTIR spectrum is displayed in Fig. S2.†

δ_H (D_2O) 0.71 (3H, t, *J* 6.8 Hz), 1.10–1.50 (22H, m), 1.57 (4H, m), 1.76 (2H, m), 2.98 (6H, s), 3.16 (4H, m), 3.39 (2H, J 6.4 Hz); δ_C (D_2O) 14.82 (1C), 22.99 (1C), 23.17 (1C), 23.57 (1C), 25.80 (1C), 26.94 (1C), 28.17 (1C), 30.01 (1C), 30.41 (1C), 30.47 (1C), 30.76 (3C), 32.88 (1C), 33.11 (1C), 35.80 (1C), 52.89 (2C), 63.11 (2C) (dioxane: δ 67.4 ppm).

2.3.3 Hydrophobic/hydrophilic modification of poly(-diallylammonium chloride) 3 with 6

*2.3.3.1 Copolymer **8a** (x = 0.8n; y = 0.2n).* To a mixture of 2.67 g (20 mmol repeating unit) of **3** in 8 mL of methanol, 0.68 g (17 mmol) of powdered NaOH was added. A white paste containing NaCl was obtained following a 30-min stirring of the mixture. Afterward, 40 mL of acetonitrile, 40 mL of toluene, and 1.83 g (4.0 mmol) of quaternary bromide **6** were added

successively. Under N_2, the mixture was heated at 70 °C for 20 h. Using a rotary evaporator, the solvents were removed at 70 °C. Furthermore, 25 mL of methanol was used to triturate the residual mixture and rotovaped once again to eradicate toluene completely. The residual mixture was transferred to a dialysis tube (MWCO: 3500 Da) using 10 mL of conc. HCl, to exchange Cl^- with Br^-, and a minimum quantity of methanol. The dialysis was continued for 24 h against distilled water. The dialyzed solution was freeze-dried to afford a creamy white solid of hydrophobically modified copolymer **8a** (3.6 g, 90%). ν_{max} (KBr): 3485, 2930, 2855, 2730, 2062, 1626, 1466, 1384, 1256, 1129, 1046, 980, 897, 728, 671, 620, and 464 cm^{-1}. FTIR spectrum is displayed in Fig. S3.†

*2.3.3.2 Copolymer **8b** (x = 0.9n; y = 0.1n).* The reaction and workup described in Section 2.3.3.1 were repeated using polymer **3** (4.0 g, 30 mmol), quaternary bromide **6** (1.37 g, 3.0 mmol), NaOH (25 mmol), acetonitrile (60 mL), and toluene (60 mL). The procedure afforded (**8b**) (4.45 g, 89%).

*2.3.3.3 Copolymer **8c** (x = 0.95n; y = 0.05n).* The above reaction and workup described in Section 2.3.3.1 were repeated using polymer **3** (4.0 g, 30 mmol), quaternary bromide **6** (0.686 g, 1.5 mmol), NaOH (25 mmol), acetonitrile (60 mL), and toluene (60 mL). The procedure afforded (**8c**) (3.97 g, 88%).

2.4 Corrosion measurements

2.4.1 Weight loss study. For weight loss (WL) experiments, mild steel coupons were cleaned using silicon carbide abrasive papers (# 120–# 1200) in a Trojan Alpha 202 polishing grinding machine. Subsequently, the polished metal specimens were cleaned with deionized water and acetone, dried, and stored in a dry place. The cleaned metal samples were weighed before being immersed in the test solutions (with and without inhibitor) for 3 h at 30 °C. After the study period had elapsed, distilled water and acetone were used to clean the mild steel samples. Finally, the metal samples were weighed again after drying. Each immersion test was triplicated, and the mean value was reported for each different inhibitor concentration. The IE (η%) of the test inhibitors was obtained using eqn (1).

$$\eta\% = \frac{w_0 - w_i}{w_0} \times 100 \quad (1)$$

where w_0 and w_i represent the weight losses of mild steel samples in the absence and presence of test inhibitors.

2.4.2 Electrochemical techniques. The electrochemical techniques were exploited using a Reference 3000 Gamry Potentiostat/Galvanostat/ZRA. A software called Echem Analyst (version: 7.8.2), developed by Gamry Instruments, was used to fit and analyze the experimental electrochemical data. The counter and reference electrodes were a graphite rod and a standard calomel electrode, respectively. To reach a steady state open circuit potential (OCP), a waiting period of 60 min was maintained before initiating any electrochemical test. To conduct the EIS experiments, the frequency range was carried from 100 kHz to 10 mHz using a small 10 mV AC signal. Charge transfer resistance values were used to calculate the IE (η_{EIS}%) using eqn (2). PDP curves were recorded by sweeping the potential (scan rate: 5 mV s^{-1}) ± 250 mV around the OCP. Upon fitting the Tafel plots, corrosion current density (i_{corr}) was obtained and was used to calculate the IE using eqn (3).

$$\eta_{EIS}\% = \frac{R_{ct}^{i} - R_{ct}^{o}}{R_{ct}^{i}} \times 100 \quad (2)$$

$$\eta_{PDP}\% = \frac{i_{corr}^{o} - i_{corr}^{i}}{i_{corr}^{o}} \times 100 \quad (3)$$

where R_{ct} implies the charge transfer resistance and i_{corr} denotes corrosion current density. On the other hand, the superscripts i and o indicate the inhibited and control solutions, respectively.

2.5 Surface tension

The surface tension of inhibitor **8b**, both with and without 2 mmol KI, was measured in the test solution. A PHYWE Surface Tensiometer (Germany), following the Du Nouy ring method, was used for this purpose. A torsion dynamometer with a front scale range of 10 mN was associated with the surface tensiometer. The tear-off force was measured with a platinum-iridium ring with a radius of 94 cm. Eqn (4) was used to find out the standard free energy of micellization.

$$\Delta G_{mic}^{o} = RT \ln(C_{CMC}) \quad (4)$$

where ΔG_{mic}^{o}, C_{CMC}, and R represent Gibbs free energy of micellization, critical micelle concentration, and molar gas constant, respectively.

2.6 Surface studies

2.6.1 X-ray photoelectron spectroscopy (XPS). A ThermoFisher™ ESCLAB™-250 QXi instrument (Al-Kα = 1486.6 eV, spot size: 650 650 μm diameter) was used for X-ray photoelectron spectroscopy (XPS) analysis. The base pressure was maintained at 10^{-10} mbar during the experiments. C 1s peak at 284.8 eV was used as the reference. Avantage software (version 5.51) was used for spectra deconvolution and peak fitting. The metal coupons for XPS analysis were cleaned as described earlier for the weight loss study. In a solution of 20% formic acid containing inhibitor **8b** and 2 mmol KI at 30 °C, the coupons were immersed for 3 h. After the study period had elapsed, distilled water was used to wash the coupons, which were then dried in an ambient air stream, followed by the analysis.

2.6.2 SEM-EDX. A Quattro ESEM-FEG integrated with energy-dispersive X-ray spectroscopy (EDX, Oxford Instruments) from ThermoFisher™ Scientific was used to examine the surface roughness of the mild steel specimens. The mild steel coupon cleaning procedure for SEM-EDX analysis was the same as discussed earlier (Section 2.6.1). Each metal coupon was gold-coated before SEM-EDX analysis was carried out.

2.7 Toxicological evaluation

The environmental friendliness of inhibitor **8b** was predicted *via* the Toxicity Estimation Software Tool (TEST) (Developer: USAEPA, version: 5.1).[32] To estimate toxicity, the software takes advantage of Quantitative Structure–Activity Relationships (QSARs). QSARs are mathematical models that use molecular descriptors, which are different chemical and physical

characteristics, to predict toxicity. In the current investigation, a widely recognized QSAR, the hierarchical clustering method, has been used to predict toxicity. This model estimates the toxicity of a given query by taking the weighted average of the predictions from several different models.

2.8 Density functional theory

Quantum chemical calculations were carried out using a single repeating unit (MW: 135.64 and 601.27 Da for **3** and **8b**, respectively) of the polymer. To fully optimize the geometries of the chemical structures, quantum chemical calculations were performed using density functional theory (DFT) at Becke-3-parameter-Lee-Yang-Par (B3LYP) level of theory and 6-31+G (d,p) as the basis set,[33] implemented in Gaussian software. The electronic properties of an inhibitor dictate how efficiently an inhibitor can undergo adsorption onto a metal surface.[34] Therefore, several important parameters, such as the energy gap between the HOMO and LUMO (ΔE), ionization energy (IE), electron affinity (EA), *etc.*, were calculated at the same level of theory. Frontier molecular orbitals (FMO) of inhibitors **3** and **8b** were visualized using Gauss View 3.0 and considered to find the molecular sights the metal surface interacts with.

3. Results and discussion

3.1 Polymer synthesis

The FTIR and NMR spectra were utilized to confirm the chemical structures of the compounds synthesized in this study. Fig. 1 shows the ^{1}H and ^{13}C NMR spectra of monocationic salt **6**. The proton, carbon count, and area integration of the proton signals confirmed the structure. Besides, the elemental analysis of quaternary ammonium salt **6** closely matches the calculated values, ensuring the synthesis of the structure. Fig. 2 and 3 depict the ^{1}H- and ^{13}C-NMR spectra of monomer **2**, cyclopolymer **3**, and modified cyclo-copolymer **8a**, respectively. The assignments of NMR peaks are based on numerous earlier works.[35–37]

The absence of residual alkene signals for monomer **2** in the ^{1}H- (Fig. 2a) and ^{13}C-NMR spectrum (Fig. 3a) can be ascribed to chain termination *via* abstraction of allylic proton and/or coupling. Each carbon marked 'a' and 'b' appeared as two signals, thereby indicating the *cis*- and *trans*-dispositions of the vicinal substituents in an approximate ratio of 3 : 1 (Fig. 3b). The presence of methyl protons and carbon (marked as 'a') in Fig. 2c and 3c confirm the incorporation of hydrophobic/hydrophilic pendant in **8a**.

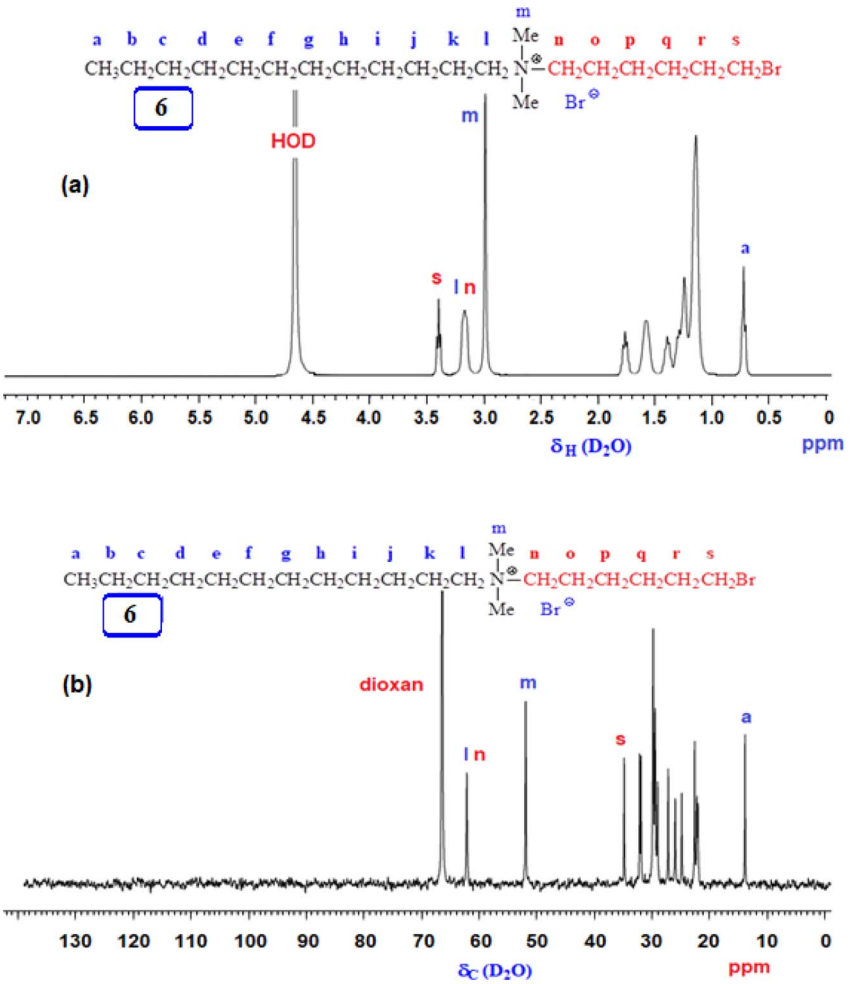

Fig. 1 (a) ^{1}H and (b) ^{13}C NMR spectra of salt **6** in D_2O.

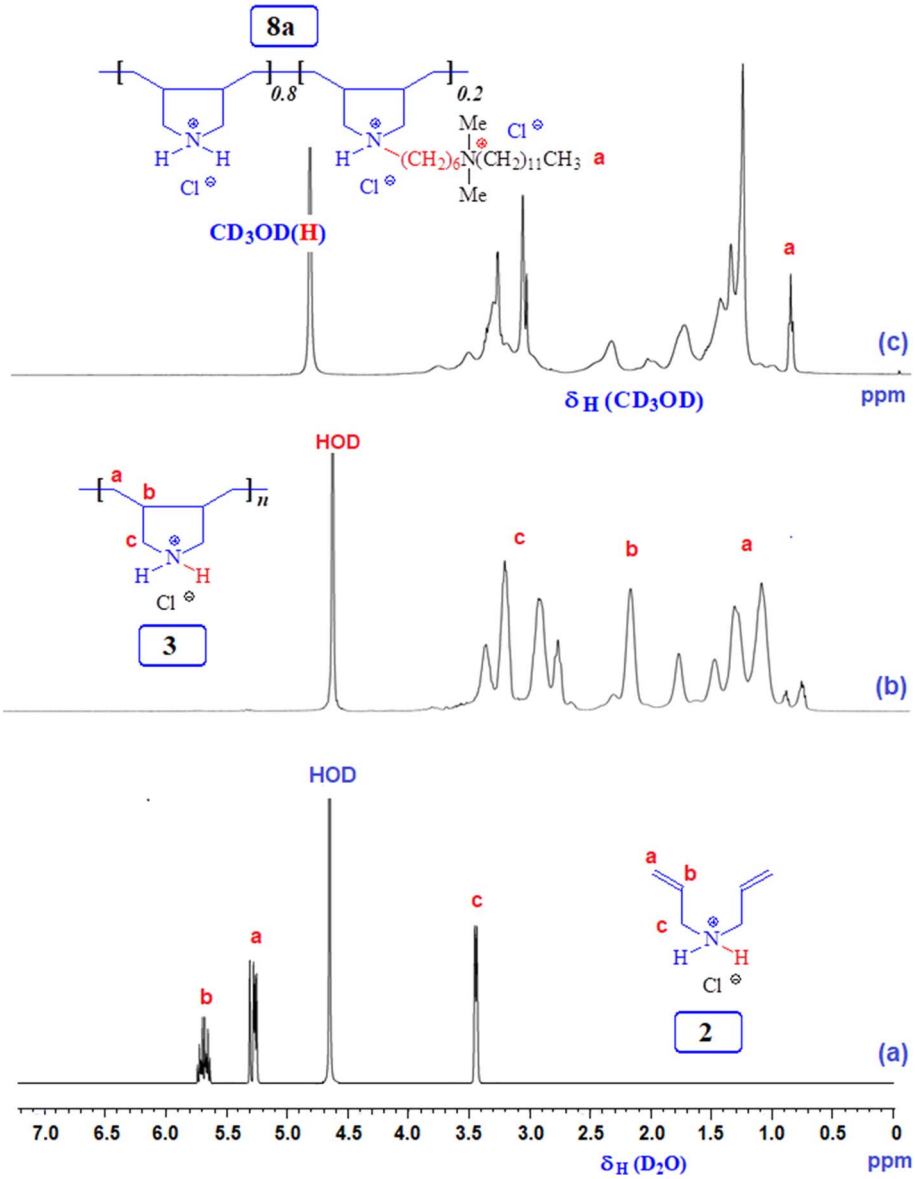

Fig. 2 ^{1}H NMR spectra of (a) **2** in D_2O, (b) **3** in D_2O, and (c) **8a** in CD_3OD.

3.2 Compositions of modified copolymers 8a, 8b, and 8c

Three modified cyclo-copolymers, **8a**, **8b**, and **8c**, with a degree of modification of 20%, 10%, and 5%, were successfully synthesized (Scheme 1). Their ^{1}H NMR spectra in D_2O are displayed in Fig. 4. Methyl protons marked 'a' can be seen in Fig. 4a–c, where the intensity of the protons decreases as the concentration of the hydrophobe is decreased from 20% (Fig. 4a) to 15% (Fig. 4b) to 5% (Fig. 4c). However, the integrations of methyl protons cannot be used to calculate the degree of modifications since the signals overlap with other signals. As illustrated in the case of **8a** in Fig. 2c, luckily, the methyl protons appeared as clear signals when CD_3OD was used as the solvent. The methyl protons of **8b** and **8c** were also found to be free of any overlapping signals in solvent CD_3OD. The degree of methyl protons incorporation was determined *via* the ^{1}H NMR spectra recorded in CD_3OD. The degree of incorporation almost matched the feed ratio of 80 : 20, 90 : 10, and 95 : 5 for **8a**, **8b**, and **8c**, respectively.

For quantitative analysis, the full relaxation of ^{1}H NMR signals (which usually have a T1 of 1 s) was ensured by employing a pulse width of 14 μs for 90° pulse (hard pulse) with a power level of 9.9 W and a delay time of 5 s. To calculate the degree of hydrophobe incorporation, the area integration of CH_3 of the hydrophobe (Fig. 2c, marked 'a') is taken as A, so the area for 1H would be $(A/3)$. The modified ring has 53 Hs (exchangeable NH is not counted), so its area integration is $53 \times (A/3)$. The total area B belongs to all the protons of both rings. So, the area for the protons in the unmodified ring becomes $B - 53 \times (A/3)$. Since the unmodified ring has 10 Hs, the area for its 1H becomes $[B - 53 \times (A/3)]/10$. The percent incorporation of the hydrophobe thus becomes:

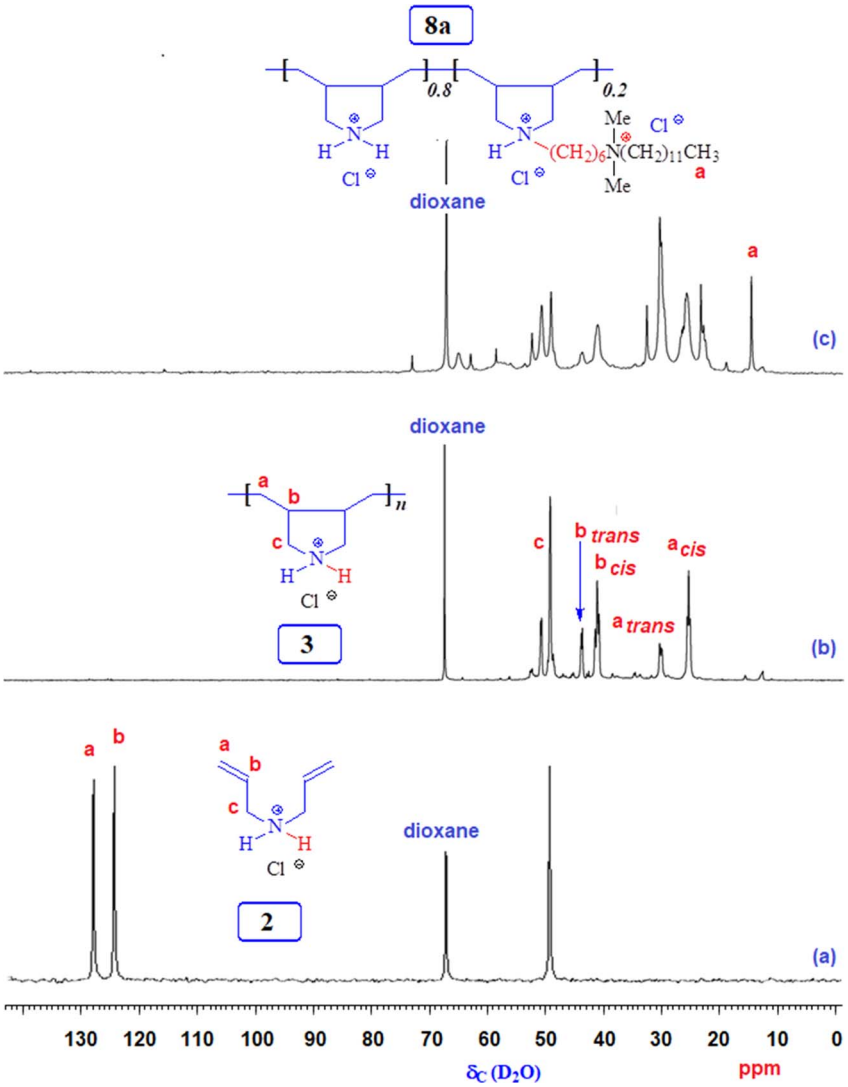

Fig. 3 ^{13}C NMR spectra of (a) **2** in D_2O, (b) **3** in D_2O, and (c) **8a** in CD_3OD.

$$\text{Mol\% hydrophobe} = \frac{\text{Area for 1H of hydrophobe}}{\text{Area of 1H of hydrphobe} + \text{Area of 1H of the ummodified ring}} = \frac{\frac{A}{3}}{\frac{A}{3} + \frac{B - \frac{53A}{3}}{10}} \times 100$$

3.3 Viscosity of the parent polymer 3 and modified cyclocopolymers 8a–c

Viscosity plots of the homopolymer and copolymers are shown in Fig. S4.† The intrinsic viscosity [η] values determined by an Ubbelohde viscometer were 0.105, 0.080, 0.121, and 0.115 dL g^{-1} for **3**, **8a** (20% incorporation), **8b** (10% incorporation), and **8c** (5% incorporation), respectively. An excessive number of hydrophobic pendants in (**8a**) presumably leads to self-micellization, thereby decreasing its hydrodynamic volume and viscosity. An increase in hydrophobe content is known to enhance intramolecular association.[38,39] In the lower hydrophobe content range, the distance between the hydrophobe units in the polymer backbone increases, thereby preventing them from undergoing intramolecular association.

3.4 Thermogravimetric analysis

Thermogravimetric (TGA) analysis of parent polymer **3** and cyclo-copolymer **8b** was studied in the 20–800 °C temperature range under N_2 flow condition (50 mL min^{-1}) and at a temperature increment of 10 °C min^{-1}. The corresponding TGA curves are shown in Fig. S5.† Both **3** and **8b** seem to be experiencing ≈5% weight loss until 250 °C. This can be attributed to polymer surfaces having some water molecules attached. Overall, the polymers are stable until 250 °C, encouraging their applications at high temperatures.

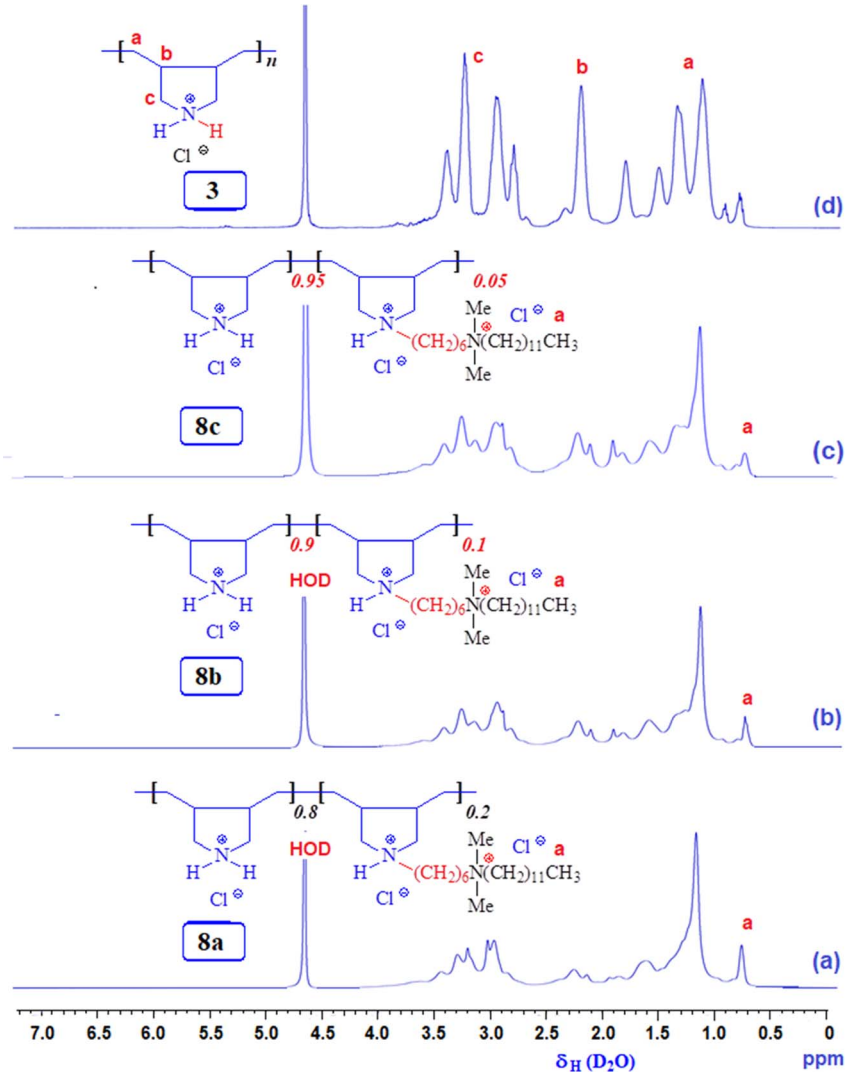

Fig. 4 ^{1}H NMR spectra of (a) **8a**, (b) **8b**, (c) **8c**, and (d) **3** in D_2O.

3.5 Weight loss studies

The efficacies of **3** and **8a–c** toward arresting mild steel corrosion at 30 °C are shown in Table 1 and Fig. 5a. The weight loss study was initially conducted at 100 ppm of inhibitors **3** and **8a–c**. It was revealed that homopolymeric corrosion inhibitor **3** imparted the lowest IE of 56.1%. On the other hand, among the three modified copolymers **8a**, **8b**, and **8c**, the order of IE was found to be **8b** (77.1%) > **8c** (67.9%) > **8a** (61.1%). The reason for modified copolymers performing better than corresponding homopolymer **3** can be attributed to copolymers containing an additional hydrophilic/hydrophobic bis-quaternary salt pendant, which has helped the copolymers to cover a larger surface area of the mild steel. On the other hand, copolymer **8a** was found to be the least efficient among all three copolymers. The presence of an excessing number (20%) of the hydrophobic pendant in **8a** has probably caused the copolymer to be less soluble and impart less IE, or the excessive hydrophobic pendant has caused a heavy crowdedness near the metal surface and didn't allow the inhibitor to undergo adsorption to a meaningful extent. Alternately, self-micellization could also have ensued before the copolymer could cover the whole surface due to an excessive hydrophobic pendant. Copolymer **8b**, with a good balance between a hydrophobic and hydrophilic portion of the chain, was found to be the most efficient of all three copolymers. Three quaternary ammonium salt moieties (NR_4^+) have facilitated excellent adsorption. The long hydrophobic chain also repelled the corrosive water molecules away from the surface. Copolymer **8c** with a 5% hydrophobic pendant was revealed to take the intermediate stance in terms of IE. Therefore, copolymer **8b** was chosen for further study on the effect of concentration on IE and corrosion rate (CR). Table 1 shows that the IE of **8b** kept increasing until 100 ppm. For 200 ppm of **8b**, IE started decreasing, which can be attributed to inhibitor desorption. As such, 100 ppm of inhibitor **8b** concentration was chosen for surface study. Fig. 5b shows the variation in mild steel corrosion rates with respect to inhibitor concentration. Reasonably, 100 ppm of **8b** decreased the CR the most.

Table 1 Weight loss study data for the use of **3** and **8a–c** as inhibitors with and without KI to retard mild steel corrosion in 20% formic acid

Sample	Conc. (ppm)	KI (mmol)	Weight loss (mg)	CR (mm year^{-1})	Surface coverage (θ)	η_{WL} (%)
Blank	—	—	45.9 ± 1.05	7.09 ± 0.16	—	—
	1	—	21.3 ± 0.95	3.29 ± 0.15	0.536	53.6 ± 1.62
	1	2	3.58 ± 0.28	0.55 ± 0.04	0.922	92.2 ± 0.44
	5	—	18.7 ± 0.20	2.89 ± 0.03	0.592	59.2 ± 0.78
	5	2	2.16 ± 0.06	0.33 ± 0.01	0.953	95.3 ± 0.17
	10	—	16.8 ± 0.15	2.60 ± 0.02	0.633	63.3 ± 0.46
	10	2	1.81 ± 0.37	0.28 ± 0.06	0.961	96.1 ± 0.82
8b	20	—	15.8 ± 0.95	2.44 ± 0.15	0.656	65.6 ± 1.25
	20	2	1.38 ± 0.21	0.21 ± 0.03	0.970	97.0 ± 0.26
	50	—	14.6 ± 0.79	2.25 ± 0.12	0.682	68.2 ± 1.20
	50	2	0.67 ± 0.12	0.10 ± 0.02	0.986	98.6 ± 0.36
	100	—	10.5 ± 0.36	1.63 ± 0.06	0.771	77.1 ± 0.29
	100	2	0.61 ± 0.03	0.09 ± 0.00	0.987	98.7 ± 0.10
	200	—	11.8 ± 0.17	1.82 ± 0.03	0.743	74.3 ± 0.92
	200	2	0.86 ± 0.05	0.13 ± 0.01	0.981	98.1 ± 0.10
5	100	—	20.2 ± 0.30	3.11 ± 0.05	0.561	56.1 ± 0.36
8a	100	—	17.8 ± 0.36	2.60 ± 0.06	0.611	61.1 ± 0.36
8c	100	—	14.7 ± 0.53	2.27 ± 0.08	0.679	67.9 ± 0.46

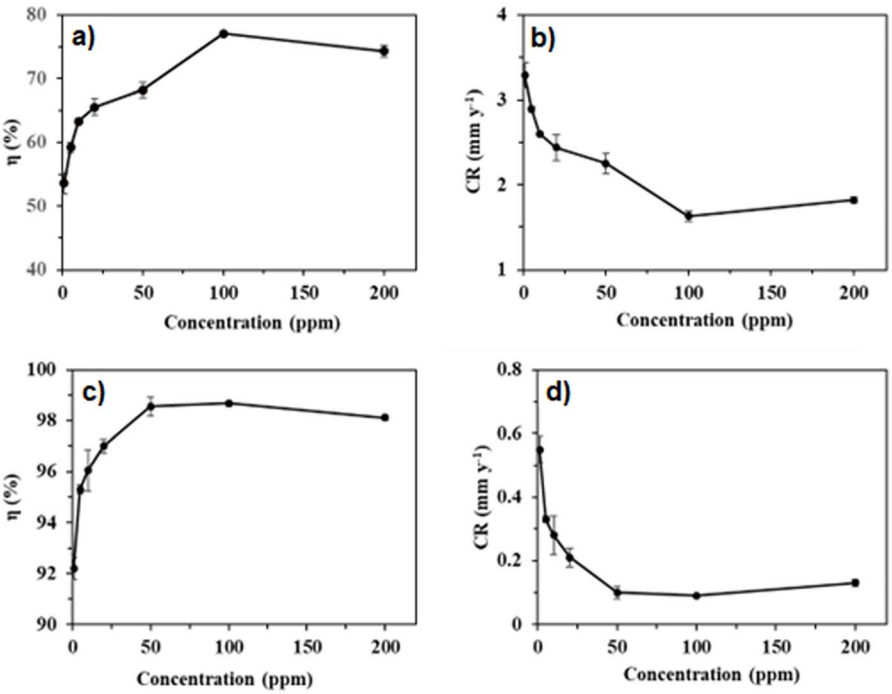

Fig. 5 Effect of inhibitor **8b** concentrations on the IE (a) and CR (b); synergistic effect of inhibitor **8b** concentrations and 2 mmol KI on the IE (c) and CR (d).

Further, the impact of 2 mmol KI as an additive on the IE of inhibitor **8b** was studied. The use of additives to enhance key inhibitors' efficacy isn't uncommon. This is also valid when the corrosive solution is much more aggressive, the study temperature is too high, or both. Halide ions are known to stabilize the adsorption of organic inhibitors. This, in turn, increases the inhibitive effect. Ascribed to the polarizability issue, I^- ion is the most effective in this regard, followed by Br^- and Cl^-.[25,26] Following the synergistic effect of 2 mmol KI, it was found that, as shown in Table 1, the IE of inhibitor **8b** increases significantly, with 1 ppm of the inhibitor and 2 mmol KI imparting more than 90% IE, which is truly remarkable. The IE of **8b** for every studied concentration increased slowly upon adding 2 mmol KI. The effect of 2 mmol KI on the IE and CR in the presence of **8b** are shown in Fig. 5c and d, respectively. In the presence of KI, the CR decreases dramatically, with the CR for the synergism of 100 ppm **8b** and 2 mmol KI reducing by 98.7% from that of control. The synergistic IE didn't increase

significantly after reaching 98.6% for 50 ppm of **8b** and 2 mmol KI. As such, this combination has been used to gain insights into surface morphologies, thermodynamic parameters, and the effect of temperature.

3.6 Adsorption isotherm

The adsorption of inhibitors, dictated by several factors, such as the structure of the inhibitor, charge distribution, the type of the metal and its surface, *etc.*, releases valuable information about the mechanism.[40] The adsorption of the inhibitor at the metal/solution interface is governed by several factors, such as the type of metal and its surface, the inhibitor structure, the charge distribution, *etc.* A few adsorption isotherms were investigated for the current study. For Langmuir adsorption isotherm, the regression of coefficient (R^2) value was found to be nearer to one, indicating that it's the best-followed isotherm. Eqn (5), where K_{ads}, C, and θ define the equilibrium constant, concentration, and surface coverage, respectively, as a mathematical expression for Langmuir adsorption isotherm. Table 2 summarizes the information obtained from all the studied isotherms. Eqn (6), where R implies molar gas constant and T highlights the experimental temperature (303 K), was used to calculate ΔG°_{ads}, or the Gibbs free energy of adsorption. The numerical value 55.5 in eqn (6) is the molar concentration of water in the test solution.

$$\frac{C}{\theta} = C + \frac{1}{K_{ads}} \quad (5)$$

$$\Delta G^{\circ}_{ads} = -RT \ln(55.5 K_{ads}) \quad (6)$$

Fig. S6† shows the Langmuir adsorption isotherm plot that was used to find K_{ads} from the intercept. The obtained value of K_{ads} was used to find the value of ΔG°_{ads} using eqn (6). The values of both K_{ads} and ΔG°_{ads} are shown in Table 2. A very high value of 2.48×10^5 L mol^{-1} for K_{ads} demonstrates the strong adsorption of inhibitor **8b** onto mild steel surfaces. The adsorption process can be regarded as physisorption or chemisorption if the absolute value of ΔG°_{ads} is less than 20 or greater than 40 kJ mol^{-1}, respectively. A mixed physi-chemisorption is considered when the absolute value of ΔG°_{ads} falls between this range.[41,42] The value of ΔG°_{ads} in the current study has been calculated to be −41.5 kJ mol^{-1}, indicating inhibitor **8b** has undergone adsorption onto mild steel *via* chemisorption. Overall, the negative sign associated with the value of ΔG°_{ads} ensures that the adsorption process is spontaneous.[19,40]

3.7 Effect of temperature and thermodynamic evaluation

Fig. 6a shows the variation in IE of KI (2 mmol) alone and **8b** (50 ppm) in the presence of 2 mmol KI measured at different time intervals of 3, 6, 12, and 24 h *via* WL technique at 60 °C. It is evident that the IE of KI remained unchanged until 12 h and then reduced drastically when measured at 24 h. On the contrary, the synergistic effect of **8b** and 2 mmol KI was so strong that its IE remained consistently close to 100% for the entire study period conducted at 60 °C. This study was carried out to point out that the contribution of KI is only to enhance the IE of **8b**. KI alone isn't enough as a corrosion inhibitor in the current investigation, as few studies are available demonstrating the usage of KI alone as a corrosion inhibitor.[43–45] To demonstrate the impact of temperatures on the IE of **8b** (100 ppm) or the corrosion rate,

Table 2 Adsorption isotherm parameters for corrosion inhibitor **8b**

	Temkin		Frumkin		Freundlich		Langmuir		
Sample	R^2	f	R^2	a	R^2	n	R^2	K_{ads} (L mol^{-1})	ΔG°_{ads} (kJ mol^{-1})
8b	0.942	22.9	0.962	13.6	0.954	0.07	0.999	2.48×10^5	−41.5

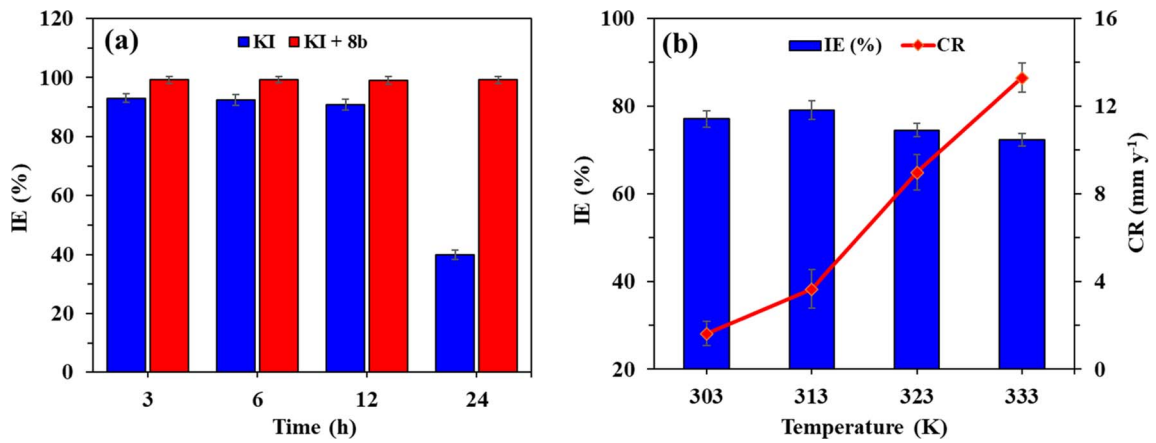

Fig. 6 (a) Variation of the IE of KI and **8b** (50 pppm) with 2 mmol KI at different time intervals at 60 °C; (b) impact of temperature (303–333 K) on the IE imparted by **8b** (100 ppm).

weight loss studies were performed at 303, 313, 323, and 333 K for 3 h. Fig. 6b shows the change of IE and corrosion rate at different temperatures; Table 3 shows various thermodynamic parameters. There is no definitive pattern in the change of IE that is quite the same over the studied temperature range while the corrosion rate increases slightly.

The corrosion rate values from different temperatures (303–313 K) can be further used to evaluate the thermodynamic parameters outlined in Table 3. Fig. S7a† shows the Arrhenius plots from which the activation energy (E_a) for the dissolution of mild steel in the presence and absence of the inhibitor was calculated using eqn (7). The transition state plots (Fig. S7b†) were obtained using eqn (8) and were used to find out the enthalpy (ΔH_{ads}) and entropy of adsorption (ΔS_{ads}) values.

$$\log \mathrm{CR} = \log A - \frac{E_a}{2.303\ RT} \tag{7}$$

$$\log \frac{CR}{T} = \left[\log\left(\frac{R}{Nh}\right) + \left(\frac{\Delta S_{ads}}{2.303\ R}\right)\right] - \frac{\Delta H_{ads}}{2.303\ RT} \tag{8}$$

where, A is the Arrhenius factor, R (universal gas constant) = 8.314 J mol^{-1} K^{-1}, h (Planck's constant) = 6.6261 × 10^{-34} J s, N (Avogadro's constant) = 6.025 × 10^{23} mol^{-1}.

The E_a values were calculated as 54.3 and 60.6 kJ mol^{-1} in the absence and presence, respectively, of **8b**, indicating that the corrosion process is more difficult in the presence of the inhibitor.[18] Reportedly, if the E_a value of the inhibited solution is greater than that of blank/control; the inhibition process is believed to follow physisorption. On the contrary, if the value of E_a for the inhibited process is equal to or less than that of blank/control, the inhibitor is believed to have undergone chemisorption.[46–48] However, some reports and findings contradict this consensus.[49,50] Nevertheless, the E_a parameter, on its own, can't decide the adsorption process. There's stiff competition between the water and inhibitor molecules for the adsorption. Therefore, displacing the water molecules from the adsorption sites takes some activation energy on the part of the inhibitor.[51] Moreover, the E_a values for the inhibited process and the blank/control aren't staggeringly different from refuting our earlier finding that inhibitor **8b** has undergone chemisorption. It has been reported that if $|\Delta H_{ads}| \leq 40$ kJ mol^{-1}, physisorption is proposed to have taken place. In contrast, chemisorption is thought to have happened for the condition: 40 kJ mol^{-1} < $|\Delta H_{ads}|$ < 100 kJ mol^{-1}.[52,53] The observed ΔH_{ads} value of 58.0 kJ mol^{-1} for the inhibited process confirms our adsorption study, finding that the inhibition process is chemisorption. Overall, the endothermic nature and bigger value of ΔH_{ads} for the inhibited process reconfirms that the corrosion phenomenon becomes more difficult when the inhibitor is present.[54] Moreover, an increase in the ΔS_{ads} value for the inhibited process means increased randomness resulting from the displacement of the water molecules by the added inhibitor.[55,56]

3.8 Potentiodynamic and linear polarization (PDP)

Fig. 7a and b show the OCP *vs.* time curves for mild steel corrosion in **8b** without and with KI, respectively. The straight OCP lines achieved after 50–60 min of dissolution indicate that the surface oxide layer was completely dissolved. It can be observed that the addition of **8b** causes the OCP curves to shift toward the more noble positive direction. The case is more prominent for the doses aided by 2 mmol KI. This clearly shows that the addition of **8b**, with and without KI, works by the adsorption of the inhibitor at the metal/solution interface. Fig. 7c shows the Tafel curves representing different concentrations of **8b** and the case where 50 ppm of **8b** was aided by 2 mmol KI. The linear segments from the anodic and cathodic curves were extrapolated to obtain several parameters, such as anodic Tafel slope (β_a), cathodic Tafel slope (β_c), current density (i_{corr}), corrosion potential (E_{corr}), *etc.* Table 4 enumerates all these parameters, and the IE (η_{PDP}) values. The i_{corr} values, as easily noticeable, were found to decrease remarkably when the inhibitor was present, confirming that the addition of the inhibitor can retard both half-cell reactions.[20,47] This downward shift is more pronounced when 2 mmol KI aids the inhibitor. When the inhibitor is used alone, the maximum η_{PDP} of 81.7% was obtained for the concentration of 100 ppm of **8b**. On the other hand, the η_{PDP} reached an amazingly high value of 99.1% for a mixture of 50 ppm **8b** and 2 mmol KI. The values of both β_a and β_c decrease with increasing inhibitor concentration regardless of 2 mmol KI addition, indicating a general change in the corrosion mechanism. A corrosion inhibitor is regarded as either anodic or cathodic when E_{corr} experiences a shift of more than 85 mV in the respective direction.[55,56] Otherwise, the inhibitor is regarded as a mixed type. Interestingly, the shift in E_{corr} doesn't exceed 85 mV when inhibitor **8b** is used alone, indicating that **8b** acts as a mixed type of inhibitor. However, when **8b** is used in the presence of 2 mmol KI, the E_{corr} values vary markedly, moving mostly toward the noble anodic direction. This implies that **8b**, in the presence of 2 mmol KI, acts as an anodic inhibitor, a case reported earlier.[57,58] Moreover, LPR experiments were carried out in the presence and absence of **8b**

Table 3 Effect of temperatures on the IE imparted by **8b** and relevant thermodynamic parameters

			E_a (kJ mol^{-1})		ΔH_{ads} (kJ mol^{-1})		ΔS_{ads} (J mol^{-1} K^{-1})	
Temp. (K)	% IE	CR (mm year^{-1})	Blank	Inhibitor **8b**	Blank	Inhibitor **8b**	Blank	Inhibitor **8b**
303	77.1	1.63	54.3	60.6	51.7	58.0	−57.3	6.84
313	79.1	3.67						
323	74.5	8.98						
333	72.5	13.3						

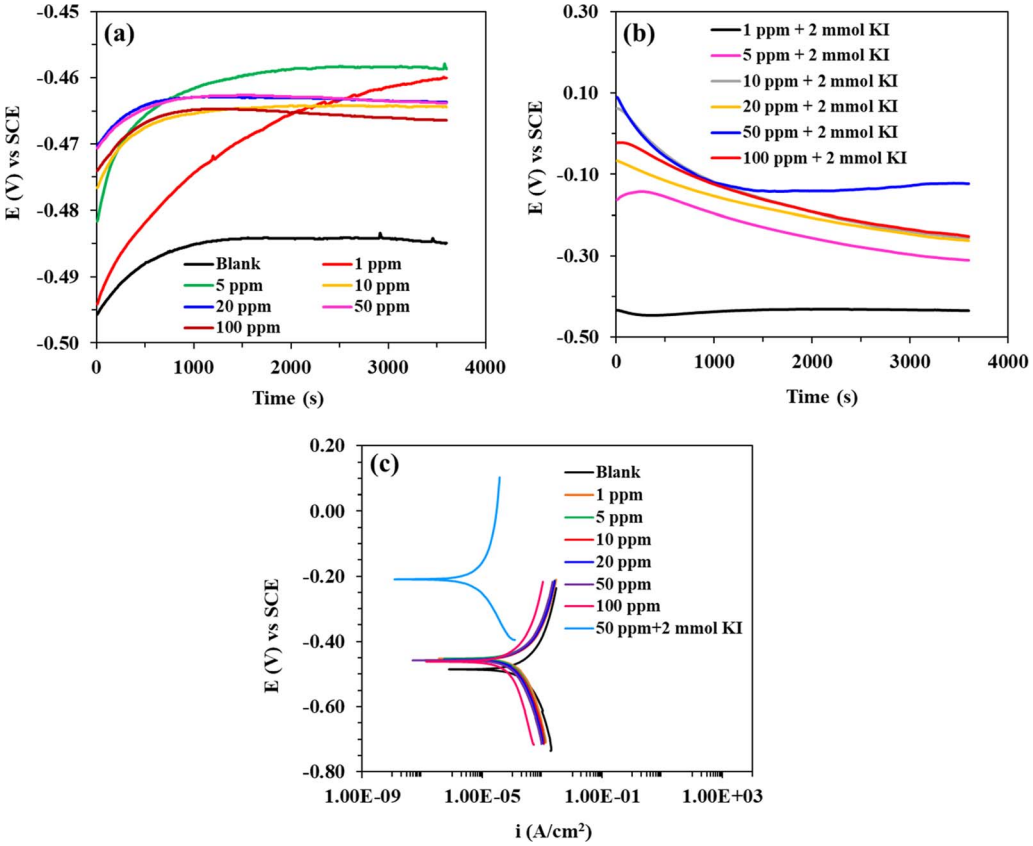

Fig. 7 OCP *vs.* time curves for mild steel corrosion in 20% formic acid containing **8b** in the (a) absence, (b) presence of 2 mmol KI, and (c) Tafel plots in the presence and absence of different concentrations of **8b** with and without 2 mmol KI.

Table 4 Potentiodynamic polarization parameters for mild steel corrosion in 20% formic acid in the presence and absence of different concentrations of **8b** and 2 mmol KI

		PDP					LPR	
Conc. (ppm)	KI (mmol)	E_{corr} (mV)	β_a (mV dec^{-1})	$-\beta_c$ (mV dec^{-1})	I_{corr} (μA cm^{-2})	η_{PDP} (%)	R_p (Ωcm^2)	η_{LPR} (%)
Blank	—	−488.6	408.6	531.4	723.3	—	142.8	—
1	—	−455.6	203.9	418.5	318.5	56.0	311.2	54.1
1	2	−449.6	115.1	237.0	46.67	93.6	1645	91.3
5	—	−455.6	210.4	408.8	284.2	60.7	358.7	60.3
5	2	−397.0	319.7	231.2	15.46	97.9	4127	96.5
10	—	−458.6	197.5	337.6	248.3	65.7	376.9	62.1
10	2	−321.8	313.0	207.5	14.38	98.0	4791	97.0
20	—	−458.6	190.3	375.3	235.7	67.4	419.8	66.0
20	2	−266.2	323.4	198.0	13.48	98.1	6550	97.8
50	—	−458.6	193.9	372.0	207.7	71.3	482.9	70.4
50	2	−209.0	243.0	170.9	6.813	99.1	9037	98.4
100	—	−461.7	245.8	440.9	131.8	81.8	701.0	79.6
100	2	−324.8	181.0	156.6	7.057	99.0	9272	98.8

and for the cases of **8b** aided by 2 mmol KI. The R_p values obtained from each line were used to find out the efficiencies (η_{LPR}). As expected, R_p values kept increasing with increasing concentration, meaning that the metal surface was experiencing more protection with increasing inhibitor concentration. Commensurately, η_{LPR} values kept increasing as well, resonating with weight loss findings and PDP studies.

3.9 Electrochemical impedance spectroscopy (EIS)

EIS is an important electrochemical technique that discloses several important information about the interface. Fig. 8a–d show the Nyquist, Bode magnitude, and phase angle plots. Table 5 shows the relevant EIS parameters, which were obtained after fitting the Nyquist and Bode plots. Fig. 8a shows the Nyquist plots corresponding to the different concentrations of

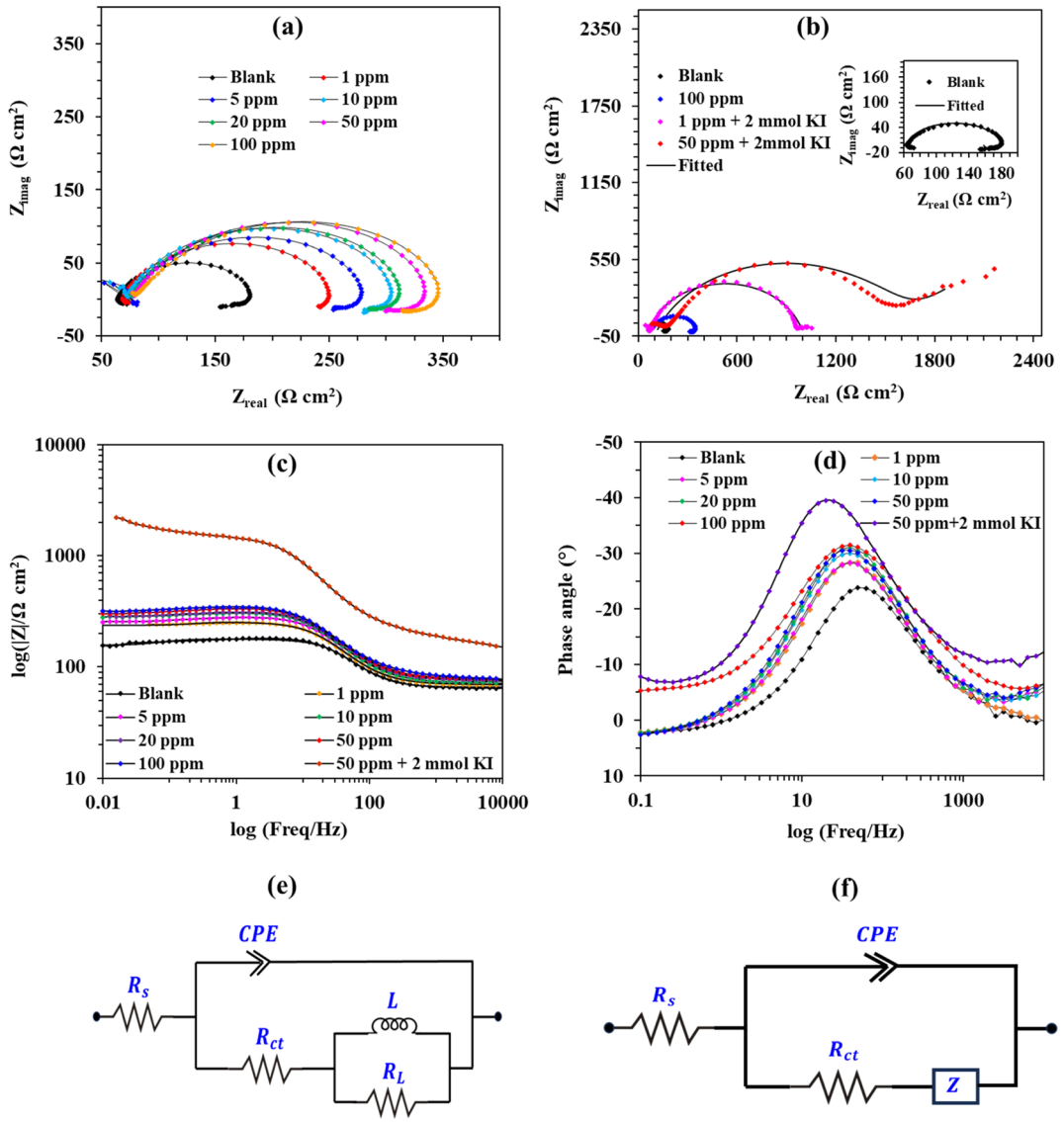

Fig. 8 (a) Nyquist plots for mild steel corrosion in 20% formic acid in the presence and absence of different concentrations of **8b**; (b) Nyquist, (c) Bode magnitude, and (d) phase angle plots for **8b** in the presence and absence of 2 mmol KI; equivalent circuits used to fit Nyquist plots associated with the usage of **8b** (e) without and (f) with KI.

8b. The plots are characterized by depressed semicircles, with the low-frequency region having an inductive loop and the high-frequency region having a capacitive loop. It is easily noticeable that adding an inhibitor causes the inductive loop to increase. The capacitive loop at the high-frequency region corresponds to the double layer and charge transfer corrosion process.

On the contrary, the inductive loop at the low frequency is ascribed to the relaxation process stemming from the interactions of the adsorbed H^+ and $HCOO^-$ ions with inhibitor species.[59,60] Fig. 8b shows the Nyquist plots for the use of 1 and 50 ppm of inhibitor **8b** in synergism with 2 mmol KI. Interestingly, when KI is used to augment the inhibitory action of **8b**, the low-frequency region shows Warburg impedance. The diameter of the semicircles is a general indication of the efficiency of an inhibitor.[18,61,62] It is visible that increasing the inhibitor concentration helped the diameter of the semicircles increase, both in the cases of inhibitor **8b** aided or not by 2 mmol KI. This gives the impression that increasing inhibitor concentration increases efficacy. A very small semicircle for 100 ppm of **8b**, as shown in Fig. 8b, in comparison to those associated with inhibitor **8b** aided by 2 mmol KI, validates the findings of the weight loss and potentiodynamic polarization studies. Fig. 8c shows the Bode magnitude plot, and Fig. 8d represents the Bode phase angle plot. Fig. 8c shows that impedance at the low-frequency side increases upon increasing the inhibitor concentrations, reaching the maximum IE for 50 ppm **8b** in the presence of 2 mmol KI. At intermediate frequencies in Bode phase angle plots, there's one time constant with one maximum, revealing that one relaxation process is happening. The values of phase angles increasing with increasing inhibitor concentrations are also another indication of increased protection.

Table 5 EIS parameters for the corrosion of mild steel in 20% formic acid in the presence and absence of different concentrations of **8b** and 2 mmol KI at 30 °C

Conc. (ppm)	KI (mmol)	L (H cm^2)	R_L (Ω cm^2)	R_{ct} (Ω cm^2)	n	C_{dl} (μF cm^{-2})	$Z_w \times 10^{-3}$ (Ω cm^2)	η (%)
Blank	—	45.17	21.82	45.13	0.917	50.78	—	—
1	—	12.98	19.53	97.99	0.782	41.90	—	53.9
1	2	—	—	845.9	0.844	21.85	179.1	94.7
5	—	24.21	31.33	111.4	0.847	39.00	—	59.5
5	2	—	—	994.1	0.769	23.87	10.07	95.5
10	—	19.96	36.95	139.1	0.801	39.56	—	67.6
10	2	—	—	1015	0.756	22.96	8.772	95.6
20	—	29.16	36.59	154.9	0.839	37.70	—	70.9
20	2	—	—	1159	0.799	20.83	11.18	96.1
50	—	42.43	43.05	175.9	0.830	37.40	—	74.3
50	2	—	—	1381	0.760	42.21	8.038	96.7
100	—	38.71	47.15	192.1	0.785	42.06	—	76.5
100	2	—	—	1460	0.800	26.71	8.327	96.9

Fig. 8e shows the circuit used to fit the Nyquist plots obtained from the immersion of mild steel in 20% formic acid containing corrosion inhibitor **8b** only. Fig. 8f shows the equivalent circuit used to fit the Nyquist plots corresponding to mild steel corrosion in the presence of **8b** and 2 mmol KI. In the circuits, R_s, R_{ct}, and W_d represent ohmic resistance, charge transfer resistance, and Warburg impedance, respectively. The inductive elements are represented by L and R_L. The double-layer capacitance, C_{dl}, is affected by the heterogeneity of the surface. Therefore, a constant phase element (CPE) is used in the circuit to replace it. The impedance of the CPE, Z_{CPE}, and the C_{dl} can be expressed in eqn (9) and (10), respectively.[59]

$$Z_{CPE} = \left(\frac{1}{Y_o}\right)\left[(j\omega)_n\right]^{-1} \quad (9)$$

$$C_{dl} = Y_o(\omega_{max})^{n-1} \quad (10)$$

where Y_o, j, ω and n denote the CPE constant, the imaginary number, the angular frequency, and frequency dispersion, respectively. The symbol ω_{max} (rad s^{-1}) represents the frequency at which the value of the imaginary impedance reaches the maximum. Frequency dispersion, also known as phase shift, results from the inhomogeneity or roughness of the solid surface.[40]

Table 5 shows that the value of R_{ct}, in comparison to that of blank, goes up with increasing inhibitor concentrations, both for the cases of **8b** used with and without KI. This confers the idea that the movement of charges across the metal/solution interfaces gets more difficult with increasing inhibitor concentration. This is another way of saying that the metal surface is experiencing more protection.[50] It is noticeable that each value of R_{ct} for inhibitor **8b** concentrations in the presence of 2 mmol KI is approximately seven to eight times higher than corresponding **8b** concentrations without 2 mmol KI. This approves of what we have seen so far: a blend of inhibitor **8b** and 2 mmol KI showing very good synergism. The increase in inhibitor concentration decreased the C_{dl} values. The reason behind this is the local dielectric constant and/or the exposed area of the metal reducing. Alternately, it can also be said that the increased thickness of the electrical double layer with increased inhibitor concentrations can also lead to a reduction in the values of C_{dl}. The increase in the values of R_{ct} or decrease in the values of C_{dl} is strong evidence for the interaction between the inhibitors and the metal surface under study.[63,64] Additionally, the values of n were found to be in the range $0.5 < n < 1$, which, reportedly, is much like that of a non-ideal polarized electrode system.[61,62]

3.10 Surface tension

The surface tension *vs.* the concentration curves for inhibitor **8b** in the presence and absence of 2 mmol KI are depicted in Fig. S8.† The critical micelle concentration (CMC) value found from extrapolating the curves is quite helpful in comparing the adsorption pattern of the inhibitor on either side of the CMC.[65] The CMC values for inhibitor **8b** were found to be 240 μmol L^{-1} (40 ppm) and 190 μmol L^{-1} (31.7 ppm) in the absence and presence of 2 mmol KI, respectively. Even before the CMC value was reached when inhibitor **8b** was used alone, a considerable portion of the surface was already covered, which was approximately 80% of the maximum IE shown by the inhibitor. Even before the micellization has ensued, a uniform adsorption layer has been constructed already. After that, micelles can adsorb more to form multilayers that provide more protection. The ΔG°_{ads} values were calculated to be −23.1 kJ mol^{-1} and −23.7 kJ mol^{-1} for inhibitor **8b** in the absence and presence of 2 mmol KI, respectively. Adsorption isotherm study (*vide supra*) showed that the ΔG°_{ads} value for inhibitor **8b** in the absence of 2 mmol KI was −41.5 kJ mol^{-1}, a value that is much more negative than that of ΔG°_{ads} for the same inhibitor, which suggested the formation of a monolayer surface before micellization occurs at the metal surface.[18]

3.11 Surface morphology

3.11.1 XPS. Fig. 9a shows the XPS survey spectra for the mild steel specimen that was kept immersed in 20% formic containing 100 ppm of **8b** at 30 °C for 3 h. It shows the presence

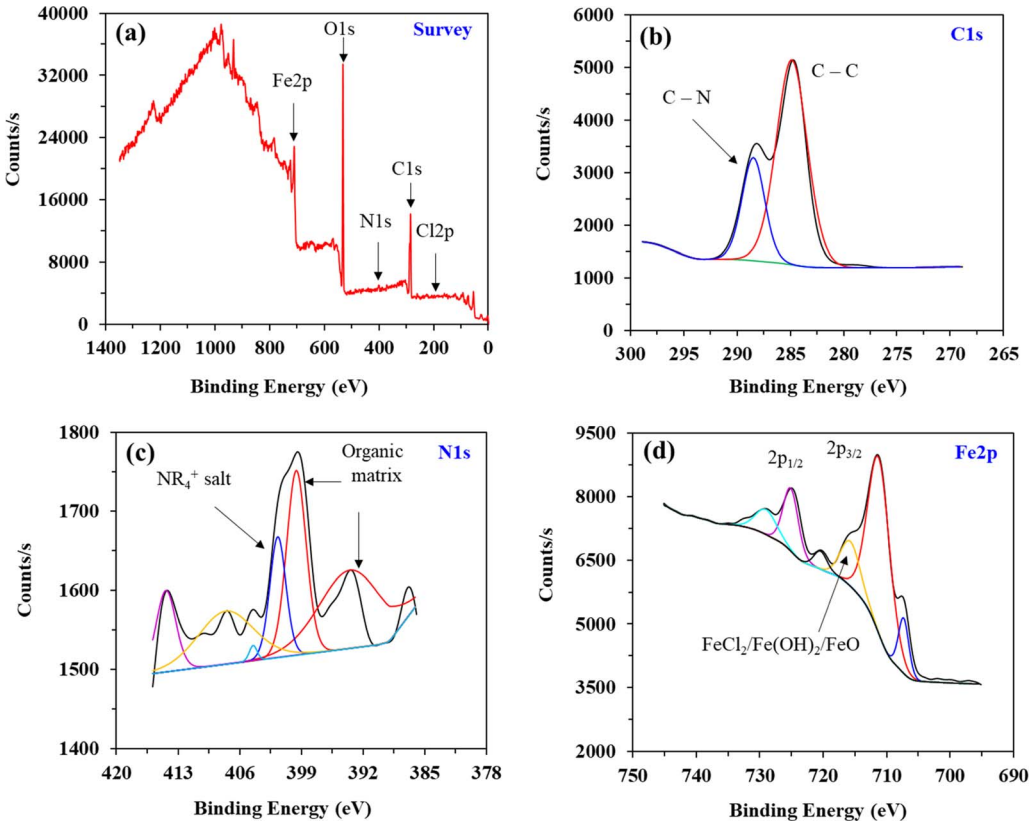

Fig. 9 XPS survey (a) and deconvoluted C 1s (b), N 1s (c), and Fe 2p (d) spectra for mild steel corrosion in 20% formic acid containing 100 ppm of **8b** at 30 °C.

of C 1s, N 1s, and Cl 2p peaks, indicating successful adsorption of **8b**. Additional peaks of Fe 2p and O 1s appear from the mild steel specimen and corrosive 20% formic acid solution, respectively. The deconvoluted spectra of C 1s, N 1s, and Fe 2p are depicted in Fig. 9b–d, respectively. Some additional information, such as peak assignments, peak binding energy, and atom% afforded *via* XPS deconvolution, are enumerated in Table 6. A dominant peak at 284.78 eV with 72.77 atom% corresponding to C–C in Fig. 9b is strong evidence of inhibitor **8b** adsorption.[61,66]

Furthermore, another peak at 288.38 eV position relating to C–N is another confirmation of **8b** undergoing adsorption. The deconvoluted spectrum of N 1s (Fig. 9c) is somewhat exciting and confirms that inhibitor **8b** underwent chemisorption, as we found through the adsorption study. The molecular structure of **8b** shows that every nitrogen present in the compound is part of either a 2°-, 3°-, or 4°-ammonium salt moiety. However, the extent of ammonium salt present in the deconvoluted spectrum is 13.10%, as shown in Table 6. This implies that it's possible that the protons attached to 2°- and 3°-ammonium salts could be abstracted by the concentrated 20% formic acid solution, leading to the nitrogens owning either a lone pair or two now. Otherwise, the atomic% of ammonium salt would have been much higher. If this happens, these nitrogens can now undergo chemisorption onto the metal surface *via* these lone pairs on nitrogen.

Nevertheless, two other prominent peaks at 393.38 and 399.48 eV corresponding to the organic matrix confirm the adsorption of the inhibitor. Fig. 9d shows Fe $2p_{1/2}$ and $2p_{3/2}$ spin orbitals regions without satellite peaks.[67,68] Relative percentages of Fe^{2+} and Fe^{3+} from both orbitals account for approximately 45 and 55%, respectively. The binding energies at 724.98, 707.18, 715.58, and 728.88 eV are attributed to Fe^{2+}. On the other hand, the binding energy at 711.08 eV is attributed to Fe^{3+}.

Table 6 XPS peak assignments and atomic compositions for various species during mild steel corrosion in 20% formic acid containing 100 ppm **8b** at 30 °C

Species	Peak BE (eV)	Assignment	Atom%
Fe 2p	724.98	Fe–O_x	13.82
	711.08	$Fe(OH)_3/Fe_2O_3/FeCl_3$	54.69
	707.18	Fe–O_x/Fe–OH	8.03
	715.58	$FeCl_2/Fe(OH)_2/FeO$	12.29
	728.88	$FeCl_2$	7.77
	720.28	Fe/Cu	3.40
C 1s	284.78	C–C	72.97
	288.38	C–N	27.03
N 1s	393.38	Organic matrix	31.56
	399.48	Organic matrix	24.35
	401.58	NR_4^+ salt	13.10
	404.38	—	0.81
	407.48	—	20.00
	414.28	—	10.18

3.11.2 SEM-EDX. To strengthen the idea that inhibitor **8b** was adsorbed onto the mild steel specimen after it was dipped into 20% formic acid at 30 °C for 3 h, an SEM investigation was carried out to examine the surface morphologies. Fig. 10a represents the surface of a polished mild steel specimen that was not treated with 20% formic acid and didn't show any roughness, pitting, or corrosion products as expected. The corresponding EDX spectrum doesn't show any other elements except iron. On the other hand, Fig. 10b, representing a mild steel surface resulting from the immersion in the test solution having no inhibitor, shows the severity of the electrolyte attack. An extreme surface roughness that has resulted from uniform corrosion can be visible without the presence of any localized attack. The associated EDX spectrum shows a prominent presence of oxygen, carbon, and iron. The excess carbon and oxygen could be due to the formic acid corrosion.

However, upon adding 100 ppm of **8b**, the mild steel surface, represented by Fig. 10c, experiences less deterioration and shows a much better and smoother surface. Peaks for carbon and chlorine on the corresponding EDX spectrum prove that inhibitor **8b** became adsorbed on the surface. Furthermore, 2 mmol KI was added, which augmented the inhibitory action 10b (50 ppm). The metal surface (Fig. 10d) looked incredibly smooth and almost the same as the polished one. This visual inspection strongly supports the extremely high efficiency found for the synergistic effect of 50 ppm **8b** and 2 mmol KI. The emergence of a small nitrogen peak and reduction in oxygen peak intensity strongly support this remark.

3.12 Toxicology study

A toxicological study that doesn't entail unnecessary animal testing is a great way to gauge chemical compounds' ecological and health impact. Fathead minnow (*Pimephales promelas*) LC50 (96 h) is a widely recognized endpoint to assess the aquatic organisms' initial effect.[69] The LC50 value refers to the concentration (in the unit of mg L^{-1}) of a chemical that kills 50% of the test animals during the study period. Certain qualities, such as relative hardiness, tolerance of variable temperatures and harsh conditions, adaptability to controlled experimentation, *etc.*, make the Fathead minnow an ideal test organism for toxicology studies. Fathead minnow can also be found in freshwater ecosystems and uninhabitable conditions such as waste drainage sites, rendering this aquatic species a worthy candidate for toxicological studies. A Fathead minnow LC50 (96 h) test simulation for the test compound **8b** done *via* hierarchical clustering QSAR toxicity estimation method predicted the LC50 value to be 1157.99 mg L^{-1}. USEPA states that a chemical compound can be practically non-toxic if the LC50 value exceeds 100 mg L^{-1}.[70] Therefore, the test compound **8b** can be considered relatively benign. Furthermore, the mean absolute error (MAE), which is the absolute average distance between the actual data and the predicted data, for the Fathead minnow LC50 (96 h) test was 0.48, which is lower than that of the entire set (0.57). This confirms an increased confidence in the predicted value. Moreover, the developmental toxicity of the test compound **8b** was also predicted using the hierarchical clustering method. Developmental toxicity indicates whether a particular chemical can interfere with human or animal growth. The test compound **8b** was found to be a developmental non-toxicant. Bioconcentration factor (BCF) is another measure of how threatening a chemical is towards aquatic species, and it's a ratio of the chemical concentration in fish to that in water at a steady state. The BCF for the test compound **8b** was predicted to be 12.28 (unitless). According to REACH regulations, a chemical is bio-accumulative if its BCF value exceeds 2000 and very bio-accumulative if its BCF value exceeds 5000.[71] This implies the tested compound is very, very safe in terms of bioaccumulation.

3.13 Density functional theory

The frontier molecular orbitals and the optimized structures of the homopolymer (**3**) and copolymer (**8b**) are depicted in Fig. 11. Table 7 enlists the quantum chemical descriptors relevant to the reactivity of these molecules. A close look at the frontier molecular orbitals (Fig. 11c–f) reveals that most of the HOMO (highest occupied molecular orbital) and LUMO (lowest unoccupied molecular orbital) charge-sharing and accepting capabilities, respectively, are located around the chloride counter ions and quaternary nitrogen moieties, observed in some earlier studies.[18–20] The phenomena of donation and retrodonation, *i.e.*, charge sharing, are crucial for the bonding between metal and inhibitor.[72,73] It is evident that the chloride counterions and pyrrolidinium moieties were important for the adsorption. The remaining long hydrocarbon chain must have acted as a water-repellent and created a hydrophobic barrier.

The FMO energies, E_{HOMO} and E_{LUMO}, have been said to be the most critical parameters to determine if an inhibitor has undergone adsorption to show an anticorrosive effect.[74] An inhibitor with a high E_{HOMO} value is more likely to donate its electrons to the empty d-orbitals of the metal atoms and make coordination bonds.[18] From Table 7, we can see that E_{HOMO} of the copolymer is much higher than that of the homopolymer. Additionally, E_{LUMO} of the copolymer is much lower than that of the homopolymer, indicating that the copolymer is more potent towards accepting electrons from the metal itself. This phenomenon is known as retrodonation and is important in corrosion inhibition. It's also known that the higher the ΔE, the difference between E_{LUMO} and E_{HOMO}, the more stable the inhibitor is regarding electron donation.[75] The ΔE value of the homopolymer is much higher than that of the copolymer, which is likely to show more IE. The electron affinity (EA) values, the negative of E_{LUMO} values that showed the tendency towards accepting electrons and were higher for the copolymer. Moreover, the IE of the copolymer was much lower than that of the homopolymer, indicating that it's much easier to ionize the copolymer, and it's more likely that the copolymer will donate more electrons than the homopolymer.[76] The electronegativity, χ, is another parameter that reveals the efficacy of a corrosion inhibitor. A high value of χ is associated with low efficacy. However, the χ and the global electrophilicity index (ω) values of the copolymer are lower than those of the homopolymer. Additionally, higher global softness (σ) and lower hardness (η) values for **8b** resonate with its higher IE.[77] The ΔN value,

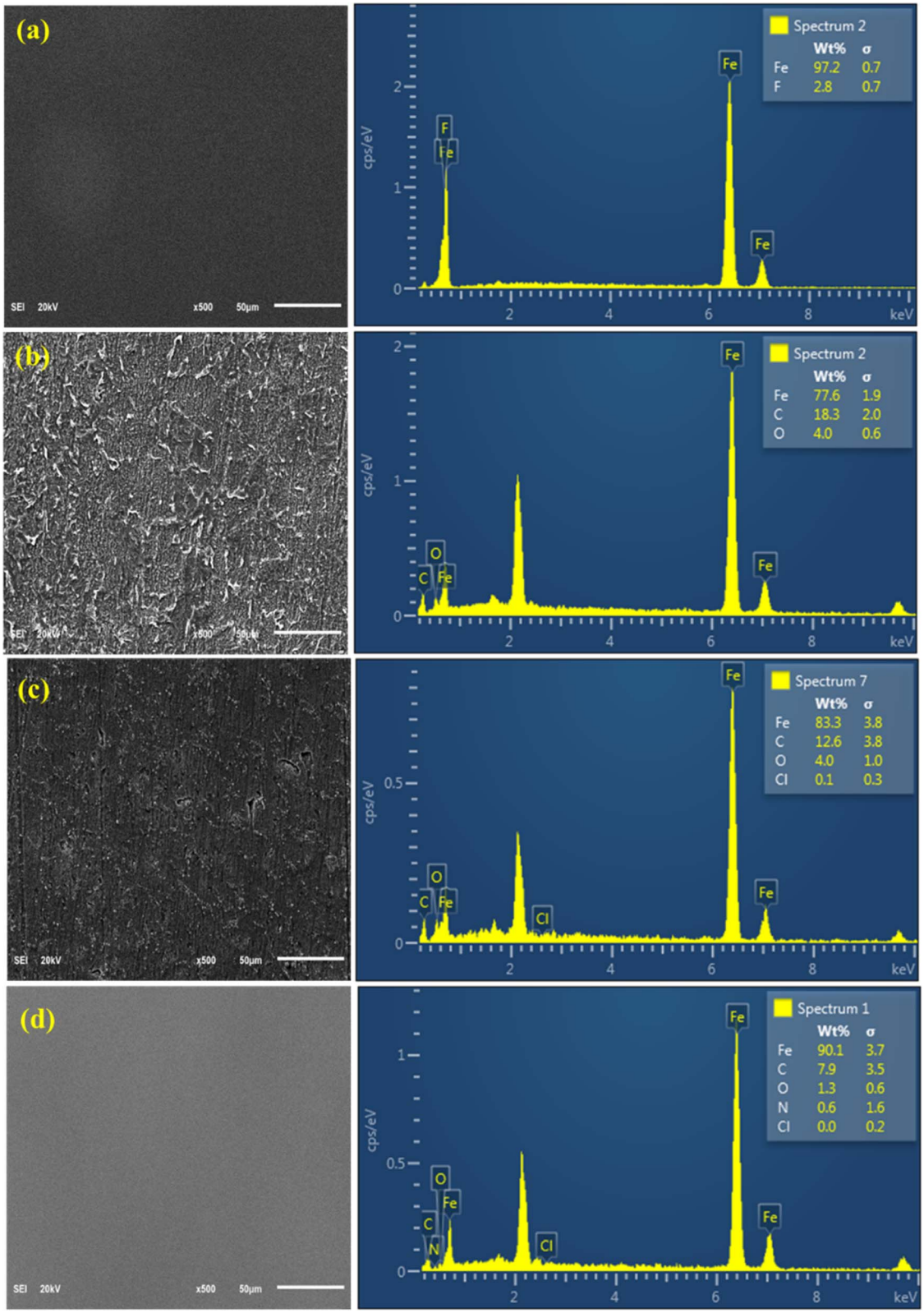

Fig. 10 Surface morphologies and EDX spectra of polished mild steel (a), mild steel corroded in the absence (b) and presence (c) of **8b**, and in the presence of **8b** and 2 mmol KI (d).

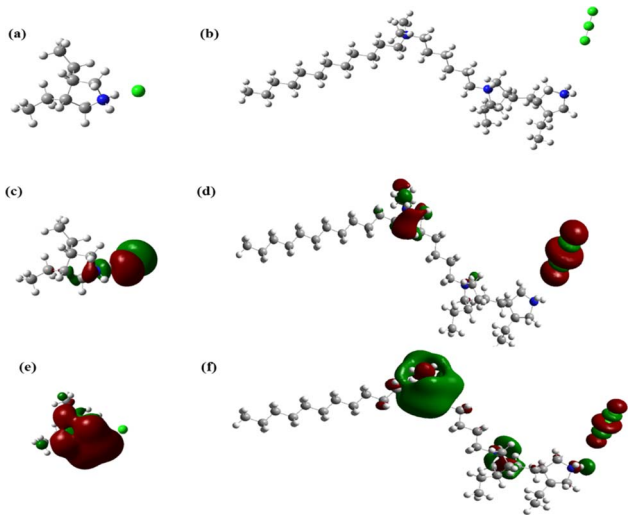

Fig. 11 Optimized structures (a and b), HOMO (c and d), and LUMO (e and f) for inhibitors 3 (left) and **8b** (right).

representing the fraction of electron transfer, of the copolymer is much, much higher than that of the homopolymer, which is another indication of its higher anticorrosion potential. Lastly, the dipole moment (μ), which indicates the overall polarity of a molecule, is also higher for the copolymer. Overall, all these DFT-optimized parameters have favored the copolymer, providing support for the experimental findings and enough incentives to explore the copolymerization of the homopolymer.

3.14 Mechanism of corrosion inhibition

XPS and SEM surface studies demonstrated that inhibitor **8b** adsorbed on the mild steel surfaces. Fig. 12 illustrates how **8b** may have undergone adsorption. DFT studies demonstrated that HOMO and LUMO regions, which indicate charge sharing and charge accepting capabilities, respectively, are located around the pyrrolidinium ring and the chloride counter ions. Since both moieties are charged species, this gives the impression that **8b** will undergo an electrostatic interaction with the positively charged metal surface to cause physical adsorption. However, adsorption and thermodynamic studies found the ΔG°_{ads} and ΔH^{o}_{ads} values to be −41.5 kJ mol^{-1} and 58.0 kJ mol^{-1}, respectively. These values indicated the mode of **8b** adsorption was chemisorption or predominantly chemisorption. This could be explained by the fact we already discussed in the XPS investigation that both 2°- and 3°-nitrogen could undergo deprotonation in the test solution. Moreover, chloride and hydroxide ions present in the test solution can deprotonate the pyrrolidinium ring's nitrogen.[23] This will lead to both nitrogens having an unshared pair of electrons that can now be used to coordinate to empty the d-orbital of metal atoms. Another 4°-nitrogen atom in the compound can't undergo deprotonation and can be adsorbed *via* a physisorption mechanism.[18–20] It has been reported that the net charge of iron surface in acid is positive.[43] Therefore, without KI, the formate ions ($HCOO^-$) from 20% formic acid and the Cl^- counter ions from **8b** can be adsorbed onto the metal surface. After that, these pre-adsorbed ions can attract the inhibitor toward the metal surface for more protection. When KI is added to the electrolyte, the I^- ions can get oxidized to I_2 by dissolving oxygen in the solution (eqn (11)). Later on, the I_2 combines very fast with I^- ions to form soluble yellowish I_3^- ions (eqn (12)).[78]

$$2I^- \rightarrow I_2 + 2e \quad (11)$$

$$I_2 + I^- \rightarrow I_3^- \quad (12)$$

Both I^- and I_3^- ions can be adsorbed on the metal surface, replacing some $HCOO^-$ ions. Therefore, the addition of KI to the solution causes the surface to be more negatively charged by

Table 7 DFT parameters for inhibitors 3 and **8b**

Inhibitor	E_{HOMO} (eV)	E_{LUMO} (eV)	ΔE (eV)	IE (eV)	EA (eV)	η (eV)	χ (eV)	ω (eV)	σ (eV)	ΔN	μ
5	−5.576	0.555	6.130	5.576	−0.555	3.065	2.511	9.659	0.326	0.377	9.350
8b	−0.204	0.013	0.217	0.204	−0.013	0.108	0.096	0.0005	9.222	21.784	37.711

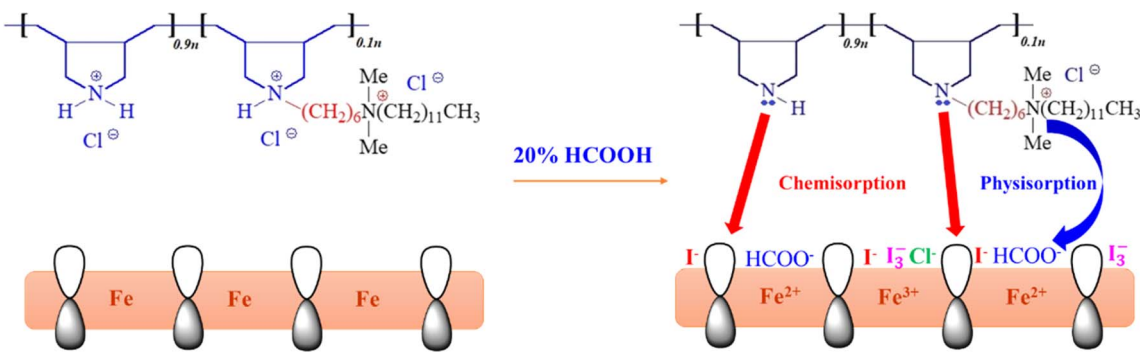

Fig. 12 An illustration of PDAAC undergoing adsorption on the mild steel surface.

creating I^- and I_3^- ions. Then this negatively charged surface containing Cl^-, $HCOO^-$, I^-, I_3^- ions will pull in the positively charged inhibitor molecule with a great force to provide excellent protection. Therefore, physisorption may have been the initial mode of interaction. However, with the successive deprotonation of the pyrrolidinum ring's nitrogens, chemisorption stands to be the dominant mode of adsorption. Electron donation from **8b** to metal atoms can cause a rise in the inter-electronic repulsion that forces the metal atoms to donate their excess electrons to unoccupied p-orbitals of the inhibitor compound, a phenomenon known as retro-donation. The hydrophobic pendant attached to the inhibitor helps to repel the water molecules away.

4. Conclusion

In the current investigation, a homopolymer, poly(-diallylammonium chloride) (**3**), has been synthesized. The homopolymer was modified by adding hydrophilic/hydrophobic bis-cationic motifs that afforded three cyclo-copolymers (**8a–c**). The synthesized compounds were characterized by IR, ^{1}H- and ^{13}C-NMR, TGA, and viscometric methods. All the synthesized polymers were then evaluated for their efficacies in mitigating mild steel corrosion in 20% formic acid. The cyclo-copolymers showed more inhibitive potential than the homopolymers. Copolymer **8b** showed the maximum IE of 81.8% for 100 ppm at 30 °C. Some explanations in support of **8b** to show better IE were offered. A good synergism between **8b** (50 ppm) and 2 mmol KI improved the IE to >99%. An extended 24 h weight loss study performed at 60 °C didn't affect the synergism at all. Adsorption isotherm studies and thermodynamic parameters were discussed in detail. With increasing inhibitor concentration, the decreasing i_{corr} values found from PDP and the increasing R_{ct} values found from EIS studies supported the findings of weight loss studies. **8b** acted as a mixed-type and an anodic inhibitor in the absence and presence of 2 mmol KI, respectively. A toxicological computational survey was performed to render the inhibitor non-toxic. XPS and SEM studies provided solid evidence for the adsorption of **8b** on the metal surface. The sights of the inhibitor interacting with the metal surface were found through DFT analysis. Excellent synergism between **8b** and KI at an elevated temperature of 60 °C can be studied further in other acid media and/or higher temperatures.

Author contributions

Lipiar K. M. O. Goni: writing – original draft, investigation, data curation, formal analysis, validation, visualization Ibrahim Y. Yaagoob: formal analysis, investigation Mohammad A. J. Mazumder: conceptualization, methodology, supervision, project administration, funding acquisition, writing – review & editing Shaikh A. Ali: conceptualization, writing – review & editing, supervision.

Conflicts of interest

There are no conflicts to declare.

Acknowledgements

The research facilities provided by King Fahd University of Petroleum & Minerals (KFUPM) under project # INAM 2112 are gratefully acknowledged. Dr Ibrahim Y. Yaagoob thankfully acknowledges the postdoctoral fellowship under the Distinguished University Professor Award (# DUP23102) provided by KFUPM.

References

1 U. M. Angst, Challenges and opportunities in corrosion of steel in concrete, *Mater. Struct.*, 2018, **51**, 4.
2 B. Liao, Z. Luo, S. Wan and L. Chen, Insight into the anti-corrosion performance of Acanthopanax senticosus leaf extract as eco-friendly corrosion inhibitor for carbon steel in acidic medium, *J. Ind. Eng. Chem.*, 2023, **117**, 238–246.
3 E. Mccafferty, *Introduction to Corrosion Science*, Springer-Verlag, New York, 2010.
4 R. Ganjoo, S. Sharma, C. Verma, M. A. Quraishi and A. Kumar, Heteropolysaccharides in sustainable corrosion inhibition: 4E (Energy, Economy, Ecology, and Effectivity) dimensions, *Int. J. Biol. Macromol.*, 2023, **235**, 123571.
5 W. Qi, Y. Huang, Y. Ma, Z. Yu and X. Zhu, Developing novel imidazoline-modified glucose derivatives as eco-friendly corrosion inhibitors for Q235 steel, *RSC Adv.*, 2023, **13**, 13516–13525.
6 A. M. Alsabagh, M. Z. Elsabee, Y. M. Moustafa, A. Elfky and R. E. Morsi, Corrosion inhibition efficiency of some hydrophobically modified chitosan surfactants in relation to their surface active properties, *Egypt. J. Pet.*, 2014, **23**, 349–359.
7 M. Salman, K. R. Ansari, J. Haque, V. Srivastava, M. A. Quraishi and M. A. J. Mazumder, Ultrasound-assisted synthesis of substituted triazines and their corrosion inhibition behavior on N80 steel/acid interface, *J. Heterocycl. Chem.*, 2020, **57**, 2157–2172.
8 R. S. Vidyarthy and P. Sivateja, Influence of activating flux tungsten inert gas welding on mechanical and metallurgical properties of the mild steel, *Mater. Today: Proc.*, 2019, **28**, 977–981.
9 M. A. Quraishi and H. K. Sharma, Thiazoles as corrosion inhibitors for mild steel in formic and acetic acid solutions, *J. Appl. Electrochem.*, 2005, **35**, 33–39.
10 M. Forslund, C. Leygraf, P. M. Claesson and J. Pan, Octadecanethiol as corrosion inhibitor for zinc and patterned zinc–copper in humidified air with formic acid, *J. Electrochem. Soc.*, 2014, **161**, C330–C338.
11 F. A. Ansari and M. A. Quraishi, Inhibitive performance of Gemini surfactants as corrosion inhibitors for mild steel in formic acid, *Port. Electrochim.*, 2010, **28**, 321–335.
12 R. C. Nascimento, L. B. Furtado, M. J. O. C. Guimarães, P. R. Seidl, J. C. Rocha, J. A. C. Ponciano and M. T. M. Cruz, Synergistic effect of propargyl alcohol, octadecylamine, and 1,3-dibutyl thiourea for API P110 alloys in acetic and formic acidic solutions used in oil well acidizing, *J. Mol. Liq.*, 2018, **256**, 548–557.

13 J. Wang, J. Liu, Q. Liu and Y. Chong, The inhibition performance of heterocyclic compounds on Q235 steel in methanol/formic acid medium: experimental and theory, *J. Mol. Liq.*, 2021, **343**, 117663.

14 Y. Boughoues, M. Benamira, L. Messaadia and N. Ribouh, Adsorption and corrosion inhibition performance of some environmental friendly organic inhibitors for mild steel in HCl solution *via* experimental and theoretical study, *Colloids Surf., A*, 2020, **593**, 124610.

15 E. A. Badr, H. H. H. Hefni, S. H. Shafek and S. M. Shaban, Synthesis of anionic chitosan surfactant and application in silver nanoparticles preparation and corrosion inhibition of steel, *Int. J. Biol. Macromol.*, 2020, **157**, 187–201.

16 S. A. Umoren, A. A. AlAhmary, Z. M. Gasem and M. M. Solomon, Evaluation of chitosan and carboxymethyl cellulose as ecofriendly corrosion inhibitors for steel, *Int. J. Biol. Macromol.*, 2018, **117**, 1017–1028.

17 C. Verma, L. K. M. O. Goni, I. Y. Yaagoob, H. Vashisht, M. A. J. Mazumder and A. Alfantazi, Polymeric surfactants as ideal substitutes for sustainable corrosion protection: a perspective on colloidal and interface properties, *Adv. Colloid Interface Sci.*, 2023, **318**, 102966.

18 B. Lyu, H. Liu, P. Li, D. Gao and J. Ma, Preparation and properties of polymeric surfactants: a potential corrosion inhibitor of carbon steel in acidic medium, *J. Ind. Eng. Chem.*, 2019, **80**, 411–424.

19 I. Y. Yaagoob, L. K. M. O. Goni, M. A. J. Mazumder, S. A. Ali, M. A. Quraishi and C. Verma, Synthesis of polymeric surfactant containing bis-cationic motifs as a highly efficient acid corrosion inhibitor for C1018 carbon steel, *New J. Chem.*, 2023, **47**, 3445–3461.

20 L. K. M. O. Goni, I. Y. Yaagoob, C. Verma, F. Almustafa, M. Y. I. Alobaid, S. A. Ali, M. A. Quraishi and M. A. J. Mazumder, Comparative corrosion inhibition performance of diallyl amine-based cyclopolymers bearing secondary, tertiary and quaternary nitrogen's motifs in 1 M HCl, *J. Mol. Liq.*, 2023, **375**, 121371.

21 A. H. Nahlé, T. J. Harvey and F. C. Walsh, Quaternary aryl phosphonium salts as corrosion inhibitors for iron in HCl, *J. Alloys Compd.*, 2018, **765**, 812–825.

22 A. E. Al-Rawajfeh and E. M. Al-Shamaileh, Inhibition of corrosion in steel water pipes by ammonium pyrrolidine dithiocarbamate (APDTC), *Desalination*, 2007, **206**, 169–178.

23 I. Y. Yaagoob, L. K. M. O. Goni, M. A. J. Mazumder, S. A. Ali, A. Alfantazi and C. Verma, Surface and interfacial properties of poly(methyldiallylammonium chloride): effect of hydrophobic pendant and synergism (KI) on corrosion of C1018CS in 15% HCl, *J. Taiwan Inst. Chem. Eng.*, 2023, **149**, 105000.

24 C. Verma, E. E. Ebenso, M. A. Quraishi and C. M. Hussain, Recent developments in sustainable corrosion inhibitors: design, performance and industrial scale applications, *Adv. Mater.*, 2021, **2**, 3806–3850.

25 A. A. Khadom, A. N. Abd and N. A. Ahmed, Synergistic effect of iodide ions on the corrosion inhibition of mild steel in 1 M HCl by *Cardaria Draba* leaf extract, *Results Chem.*, 2022, **4**, 100668.

26 N. Sait, N. Aliouane, N. Ait Ahmed, L. Toukal and M. Al-Noaimi, Synergistic effect of potassium iodide on corrosion inhibition of copper by tetraphosphonic acid in hydrochloric acid solution, *J. Adhes. Sci. Technol.*, 2022, **36**, 109–133.

27 M. M. Solomon and S. A. Umoren, Enhanced corrosion inhibition effect of polypropylene glycol in the presence of iodide ions at mild steel/sulphuric acid interface, *J. Environ. Chem. Eng.*, 2015, **3**, 1812–1826.

28 M. M. Solomon and S. A. Umoren, Performance evaluation of poly (methacrylic acid) as corrosion inhibitor in the presence of iodide ions for mild steel in H_2SO_4 solution, *J. Adhes. Sci. Technol.*, 2015, **29**, 1060–1080.

29 K. R. Ansari, D. S. Chauhan, M. A. Quraishi, A. Y. Adesina and T. A. Saleh, The synergistic influence of polyethyleneimine grafted graphene oxide and iodide for the protection of steel in acidizing conditions, *RSC Adv.*, 2020, **10**, 17739.

30 M. R. Sovizi and R. Abbasi, Effect of carboxymethyl cellulose on the corrosion behavior of aluminum in H_2SO_4 solution and synergistic effect of potassium iodide, *J. Adhes. Sci. Technol.*, 2020, **34**, 1664–1678.

31 S. A. Haladu, S. A. Umoren, S. A. Ali and M. M. Solomon, Synthesis and characterization of cyclic cationic polymer and its anti-corrosion property for low carbon steel in 15% HCl solution, *Int. J. Electrochem. Sci.*, 2017, **12**, 9061–9083.

32 U. S. EPA, *TEST 5.1 (Toxicity Estimation Software Tool)*, U.S. Environmental Protection Agency, Cincinnati, OH, 2020.

33 Z. Shariatinia and A. Ahmadi-Ashtiani, Corrosion inhibition efficiency of some phosphoramide derivatives: DFT computations and MD simulations, *J. Mol. Liq.*, 2019, **292**, 111409.

34 J. Sebhaoui, Y. E. Bakri, Y. E. Aoufir, E. H. Anouar, A. Guenbour, A. A. Nasser and E. M. Essassi, Synthesis, NMR characterization, DFT and anti-corrosion on carbon steel in 1 M HCl of two novel 1,5-benzodiazepines, *J. Mol. Struct.*, 2019, **1182**, 123–130.

35 S. R. Johns, R. I. Willing, S. Middleton and A. K. Ong, Cyclopolymerization. VII. The ^{13}C NMR spectra of cyclopolymers obtained from *N*,*N*-diallyamines, *J. Macromol. Sci., Part A*, 1976, **10**, 875–891.

36 J. E. Lancaster, L. Baccei and H. P. Panzer, The structure of poly(diallyldimethyl-ammonium) chloride by ^{13}C-NMR spectroscopy, *J. Polym. Sci., Polym. Lett. Ed.*, 1976, **14**, 549–555.

37 I. Y. Yaagoob, M. K. Aldahdooh, A. A. Al-Taq, H. A. Al-Muallem, M. A. J. Mazumder and S. A. Ali, Synthesis of stimuli-responsive ionic cyclopolymers in search of phosphorous-free antiscalants, *J. Appl. Polym. Sci.*, 2021, **138**, 50402.

38 Y. Chang and C. L. McCormick, Water-soluble copolymers: 57. Amphiphilic cyclocopolymers of diallylalkoxybenzyl-methylammonium chloride and diallyl-dimethylammonium chloride, *Polymer*, 1994, **35**, 3503–3512.

39 S. A. Ali, Y. Umar and B. F. Abu-Sharkh, Amphiphilic cycloterpolymers of diallyldimethylammonium chloride,

diallyloctadecylammonium chloride and sulfur dioxide, *J. Appl. Polym. Sci.*, 2005, **97**, 1298–1306.

40 R. K. Mehta, M. Yadav and I. B. Obot, Electrochemical and computational investigation of adsorption and corrosion inhibition behavior of 2-aminobenzohydrazide derivatives at mild steel surface in 15% HCl, *Mater. Chem. Phys.*, 2022, **290**, 126666.

41 S. K. Gupta, R. K. Mehta, N. Kumari, M. Yadav and I. B. Obot, Study on benzylidine derivatives as corrosion inhibitors for mild steel in 15% HCl medium: experimental & theoretical investigation, *J. Phys. Chem. Solids*, 2023, **183**, 111632.

42 U. Mamudu, M. S. Alnarabiji and R. C. Lim, Adsorption isotherm and molecular modeling of phytoconstituents from *Dillenia suffruticosa* leaves for corrosion inhibition of mild steel in 1.0 M hydrochloric acid solution, *Results Surf. Interfaces*, 2023, **13**, 100145.

43 A. A. Khadom, A. N. Abd and N. A. Ahmed, Potassium iodide as a corrosion inhibitor of mild steel in hydrochloric acid: kinetics and mathematical studies, *J. Bio- Tribo-Corros.*, 2018, **4**, 17.

44 A. S. Yaro, A. A. Khadom and S. M. Lahmod, Kinetics of the corrosion inhibition reaction of steel alloys in acidic media by potassium iodide, *React. Kinet., Mech. Catal.*, 2013, **109**, 417–432.

45 S. H. Sanad, A. A. Ismail and N. A. Mahmoud, Inhibition effect of potassium iodide on corrosion of stainless steel in hydrochloric acid solution, *J. Mater. Sci.*, 1992, **27**, 5706–5712.

46 S. Masroor, M. Mobin, A. K. Singh, R. A. K. Rao, M. Shoeb and M. J. Alam, Aspartic di-dodecyl ester hydrochloride acid and its ZnO-NPs derivative, as ingenious green corrosion defiance for carbon steel through theoretical and experimental access, *SN Appl. Sci.*, 2020, **2**, 144.

47 N. A. Odewunmi, M. A. J. Mazumder, S. A. Ali and I. B. Obot, 1,12-Dodecyldiyl-bis(dimethylalkylammonium bromide) compounds anticorrosion property on C1018/15% HCl solution interface: experimental, molecular dynamics simulation, and DFT studies, *J. Mol. Liq.*, 2022, **346**, 118332.

48 N. A. Odewunmi, M. A. J. Mazumder and S. A. Ali, Tipping effect of tetra-alkylammonium on the potency of N-(6-(1H-benzo[d]imidazole-1-yl)hexyl)-N, N-dimethyldodecan-1-aminium bromide (BIDAB) as corrosion inhibitor of austenitic 304L stainless steel in oil and gas acidization: experimental and DFT approach, *J. Mol. Liq.*, 2022, **360**, 119431.

49 M. Yadav, D. Behera and U. Sharma, Nontoxic corrosion inhibitors for N80 steel in hydrochloric acid, *Arabian J. Chem.*, 2016, **9**, S1487–S1495.

50 A. Yurt, A. Balaban, S. U. Kandemir, G. Bereket and B. Erk, Investigation on some Schiff bases as HCl corrosion inhibitors for carbon steel, *Mater. Chem. Phys.*, 2004, **85**, 420–426.

51 K. R. Ansari, M. A. Quraishi and A. Singh, Pyridine derivatives as corrosion inhibitors for N80 steel in 15% HCl: electrochemical, surface and quantum chemical studies, *Measurement*, 2015, **76**, 136–147.

52 J. Haque, K. R. Ansari, V. Srivastava, M. A. Quraishi and I. B. Obot, Pyrimidine derivatives as novel acidizing corrosion inhibitors for N80 steel useful for petroleum industry: a combined experimental and theoretical approach, *J. Ind. Eng. Chem.*, 2017, **49**, 176–188.

53 S. K. Shukla and E. E. Ebenso, Corrosion inhibition, adsorption behavior and thermodynamic properties of streptomycin on mild steel in hydrochloric acid medium, *Int. J. Electrochem.*, 2011, **6**, 3277–3291.

54 N. M. El Basiony, A. Elgendy, A. E. El-Tabey, A. M. Al-Sabagh, G. M. Abd El-Hafez, M. A. El-raouf and M. A. Migahed, Synthesis, characterization, experimental and theoretical calculations (DFT and MC) of ethoxylated aminothiazole as inhibitor for X65 steel corrosion in highly aggressive acidic media, *J. Mol. Liq.*, 2020, **297**, 111940.

55 P. K. Paul, M. Yadav and I. B. Yadav, Investigation on corrosion protection behavior and adsorption of carbohydrazide-pyrazole compounds on mild steel in 15% HCl solution: electrochemical and computational approach, *J. Mol. Liq.*, 2020, **314**, 113513.

56 N. Tiwari, R. K. Mitra and M. Yadav, Corrosion protection of petroleum oil well/tubing steel using thiadiazolines as efficient corrosion inhibitor: experimental and theoretical investigation, *Surf. Interfaces*, 2021, **22**, 100770.

57 M. Tang, X. Li, S. Deng and R. Lei, Synergistic inhibition effect of *Mikania micrantha* extract with KI on steel corrosion in H_2SO_4 solution, *J. Mol. Liq.*, 2021, **344**, 117926.

58 J. Tan, L. Guo, H. Yang, F. Zhang and Y. El Bakri, Synergistic effect of potassium iodide and sodium dodecyl sulfonate on the corrosion inhibition of carbon steel in HCl medium: a combined experimental and theoretical investigation, *RSC Adv.*, 2020, **10**, 15163–15170.

59 K. C. D. S. D. Lima, V. M. Paiva, D. Perrone, B. Ripper, G. Simões, M. L. M. Rocco, A. G. D. Veiga and E. D'Elia, Glycine max meal extracts as corrosion inhibitor for mild steel in sulphuric acid solution, *J. Mater. Res. Technol.*, 2020, **9**, 12756–12772.

60 I. B. D. Barros, M. A. A. Kappel, P. M. D. Santos, V. F. D. V. Junior, E. D'Elia and I. N. Bastos, The inhibitory action of *Bauhinia purpurea* extracts on the corrosion of carbon steel in sulfuric acid medium, *Mater. Res.*, 2016, **19**, 187–194.

61 N. A. Odewunmi, M. A. J. Mazumder and S. A. Ali, Tipping effect of tetra-alkylammonium on the potency of N-(6-(1H-benzo[d]imidazole-1-yl)hexyl)-N, N-dimethyldodecan-1-aminium bromide (BIDAB) as corrosion inhibitor of austenitic 304L stainless steel in oil and gas acidization: experimental and DFT approach, *J. Mol. Liq.*, 2022, **360**, 119431.

62 B. Liao, S. Ma, S. Zhang, X. Li, R. Quan, S. Wan and X. Guo, Fructus cannabis protein extract powder as a green and high effective corrosion inhibitor for Q235 carbon steel in 1 M HCl solution, *Int. J. Biol. Macromol.*, 2023, **239**, 124358.

63 S. E. H. Etaiw, G. S. Hassan, A. A. El-Hossiany and A. S. Fouda, Nano-metal–organic frameworks as corrosion inhibitors for strengthening anti-corrosion behavior of

carbon steel in a sulfuric acid environment: from synthesis to applications, *RSC Adv.*, 2023, **13**, 15222–15235.

64 X. Luo, C. Ci, C. Zhou, J. Li, W. Xiong, Z. H. Xie, M. Guo, D. Wu, B. Chen and Y. Liu, Dopamine modified natural glucomannan as a highly efficient inhibitor for mild steel: experimental and theoretical methods, *Int. J. Biol. Macromol.*, 2023, **242**, 124712.

65 V. N. Ayukayeva, G. I. Boiko, N. P. Lyubchenko, R. G. Sarmurzina, R. F. Mukhamedova, U. S. Karabalin and S. A. Dergunov, Polyoxyethylene sorbitan trioleate surfactant as an effective corrosion inhibitor for carbon steel protection, *Colloids Surf., A*, 2019, **579**, 123636.

66 E. A. Flores, O. Olivares, N. V. Likhanova, M. A. Domínguez-Aguilar, N. Nava, D. Guzman-Lucero and M. Corrales, Sodium phthalamates as corrosion inhibitors for carbon steel in aqueous hydrochloric acid solution, *Corros. Sci.*, 2011, **53**, 3899–3913.

67 D. Wilson and M. A. Langell, XPS analysis of oleylamine/oleic acid capped Fe_3O_4 nanoparticles as a function of temperature, *Appl. Surf. Sci.*, 2014, **303**, 6–13.

68 B. Andrzejewskia, K. Chybczyńska, B. Hilczer, M. Błaszyk, T. Luciński, M. Matczak and L. Kępiński, Controlled growth of bismuth ferrite multiferroic flowers, *Mater. Sci.*, 2014, **1402**, 1336, DOI: **10.48550/arXiv.1402.1336**.

69 C. L. Russom, S. P. Bradbury, S. J. Broderius, D. E. Hammermeister and R. A. Drummond, Predicting modes of toxic action from chemical structure: acute toxicity in the fathead minnow (*Pimephales Promelas*), *Environ. Toxicol. Chem.*, 1997, **16**, 948–967.

70 United States Environmental Protection Agency (USEPA), **https://www3.epa.gov/pesticides/endanger/litstatus/effects/redleg-frog/naled/appendix-i.pdf** accessed December 2023.

71 M. I. Petoumenou, F. Pizzo, J. Cester, A. Fernández and E. Benfenati, Comparison between bioconcentration factor (BCF) data provided by industry to the European Chemicals Agency (ECHA) and data derived from QSAR models, *Environ. Res.*, 2015, **142**, 529–534.

72 D. K. Verma, R. Aslam, J. Aslam, M. A. Quraishi, E. E. Ebenso and C. Verma, Computational modeling: theoretical predictive tools for designing potential organic corrosion inhibitors, *J. Mol. Struct.*, 2021, **1236**, 130294.

73 C. Fu, C. Liu, T. Li, X. Zhang, F. Wang, J. Yang, Y. Jiang, P. Cui and H. Li, DFT calculations: a powerful tool for better understanding of electrocatalytic oxygen reduction reactions on Pt-based metallic catalysts, *Comput. Mater. Sci.*, 2019, **170**, 109202.

74 I. Arshad, K. Qureshi, A. S. Saleemi, A. Abdullah, A. A. A. Bahajjaj, S. Ali and A. Bokhari, Melamine–isatin tris Schiff base as an efficient corrosion inhibitor for mild steel in 0.5 molar hydrochloric acid solution: weight loss, electrochemical and surface studies, *RSC Adv.*, 2023, **13**, 19301–19311.

75 D. S. Chauhan, K. R. Ansari, A. A. Sorour, M. A. Quraishi, H. Lgaz and R. Salghi, Thiosemicarbazide, and thiocarbohydrazide functionalized chitosan as ecofriendly corrosion inhibitors for carbon steel in hydrochloric acid solution, *Int. J. Biol. Macromol.*, 2018, **107**, 1747–1757.

76 N. Baildya, N. N. Ghosh and A. P. Chattopadhyay, Anti-corrosive properties of quercetin and its derivatives on Fe (111) surface: a quantum chemical approach, *SN Appl. Sci.*, 2019, **1**, 735.

77 M. Rbaa, M. Fardioui, C. Verma, A. S. Abousalem, M. Galai, E. E. Ebenso, T. Guedira, B. Lakhrissi, I. Warad and A. Zarrouk, 8-Hydroxyquinoline based chitosan derived carbohydrate polymer as biodegradable and sustainable acid corrosion inhibitor for mild steel: experimental and computational analyses, *Int. J. Biol. Macromol.*, 2020, **155**, 645–655.

78 S. Cao, D. Liu, H. Ding, J. Wang, H. Lu and J. Gui, Corrosion inhibition effects of a novel ionic liquid with and without potassium iodide for carbon steel in 0.5 M HCl solution: an experimental study and theoretical calculation, *J. Mol. Liq.*, 2019, **275**, 729–740.